CONSTRAINTS ON THE VISCOSITY OF THE EARTH'S MANTLE BENEATH THE SOUTH PACIFIC

by

Susan Aileen Evans

B.A., Geophysical Sciences
The University of Chicago, 1991

Submitted to the Department of
Earth, Atmospheric, and Planetary Sciences
in Partial Fulfillment of the Requirements for the Degree of

Master of Science in Geophysics

at the
Massachusetts Institute of Technology
September 1994

Signature of Author_____
Department of Earth, Atmospheric, and Planetary Sciences
September, 1994

Certified by_____
Marcia K. McNutt
Thesis Advisor

Accepted by_____
Thomas H. Jordan
Department Head

Abstract

The South Pacific Superswell contains a disproportionate number of volcanic islands and is characterized by a long-wavelength topographic swell, a negative geoid anomaly, and slower than average seismic velocities within the upper mantle. Assuming that these regions of slow seismic velocity correspond to hot, buoyant material deriving convection in a viscous mantle, the requirement that they produce a positive depth anomaly but a negative geoid anomaly places strong constraints on the viscosity structure of the mantle beneath the South Pacific. We examine viscosity profiles which have been previously determined using global long-wavelength geoid data, but none adequately satisfies the geoid and topography in the Superswell. The presence of slow seismic velocities in the uppermost mantle suggests that hot, and therefore less viscous material lies beneath the lithosphere. To explore the possibility that the uppermost mantle is less viscous beneath the Superswell, we search for variants of global viscosity models which satisfy the data.

We have developed an algorithm for inverting seismic velocity, depth anomalies, and geoid directly for the radial viscosity structure of the mantle for a limited spatial region. We form an iterative scheme to determine the viscosity solution which minimizes the misfit to the data, yet is closest in a least-squares sense to a reference viscosity model, such as that derived from global modeling of long wavelength geoid. This technique performs well in tests using synthetic data; in most cases, the procedure determines a known viscosity profiles to within 15%.

We perform inversions with the observed geoid and topography data for the Superswell for eleven different reference viscosity models. Seventeen viscosity solutions are obtained and grouped into five classes of viscosity models. Although these models predict similar misfits to the data, they predict substantially different geoid fields and only two solutions are consistent with both sets of data. One solution possesses a low viscosity zone between 100 and 400 km depth, with a factor of 12 increase in viscosity at the top of the transition zone, and again at 670 km. The other model contains a low viscosity layer between 670 and 1000 km depth. Although both models satisfy the geoid and topography data equally well, we prefer the first model because the depth of the low viscosity layer coincides with the depth of the strongest seismically-inferred temperature variations, providing a physical explanation for the lower viscosities.

Acknowledgements

There are many people to whom I am grateful for making my stay here at MIT a very positive experience.

First of all, many thanks to Sean Solomon for his support during my first two years in graduate school and for introducing me to the world of academic research. I'm grateful to Marcia McNutt for taking over where he left off and for supervising this thesis. Thanks to Brad Hager for several fruitful discussions and for sharing his kernel code.

I will always be grateful to my fellow students who have created such a supportive environment in the department and who have helped make my stay here enjoyable. I want to thank the extraterrestrials of the 5th floor (Pat McGovern, Nori Namiki, and Mark Simons) for many thought-provoking discussions of Venus tectonics. They also kept me on my toes, as often I was taken unawares by one of their spontaneous ludicrous remarks. Mark deserves special thanks for numerous helpful discussions and for generously sharing his spherical harmonic code. I will always be grateful to Mousumi Roy for her ever-present smile and willingness to go for coffee at all hours. Thanks to Svetlana Panasyuk for many fruitful discussions on mantle dynamics and other life philosophies. I'd like to thank Paula Waschbush for helpful discussions and for furnishing the Boston Globe to provide me with my daily comics fix. I'll always remember Gretchen Eckhardt for our many intriguing discussions on minerals, gemstones, geometries and snowflakes. Thanks to Libby Kurten, Marie Senat, Cynthia Hanes, and Deb Sykes for shielding me from the MIT bureaucracy and for numerous neighborly chit-chats. Thanks to Steve Shapiro for sharing his knowledge of the intricacies of UNIX and Fortran., and to my office mates: Jim Gaherty, Mamoru Kato, and Sang-Mook Lee for several helpful discussions and for sharing their libraries.

I'm very grateful to my brother Dennis and sister-in-law Susan for providing me with a New Hampshire retreat whenever I needed to get away, and to my nieces: Devon, Hannah, and Cass for reminding me what life is really about. Finally, I want to thank my husband, Jeff, for all of his love and support over the past three years. I couldn't have done it without you.

Table Of Contents

Chapter 1: Introduction

The seafloor beneath most of the world's oceans deepens away from mid-ocean ridges in a predictable manner; its depth is related to the square root of the lithospheric age [*Parsons and Sclater*, 1977; *Stein and Stein*, 1992]. While this model is consistent with seafloor depths and heat flow measurements throughout most of the world's ocean basins, the lithosphere beneath French Polynesia deviates from the predictions of this model. The seafloor is too shallow compared to the 125-km-thick plate model of *Parsons and Sclater* [1977], and the geoid is too negative. In addition, seismic models indicate slower than average shear wave velocities e.g. *Su et al.* [1994], and absolute plate velocities reach a global high over this region [*Minster and Jordan*, 1978; *DeMets et al.*, 1990]. Based on these observations, the lithosphere and/or asthenosphere beneath French Polynesia appears to be anomalous with respect to other oceanic regions of similar age.

McNutt and Fischer [1987] termed this region the South Pacific Superswell and attributed its anomalous properties to an unusually thin 75-km-thick thermal lithosphere. While a thin lithosphere is consistent with the observed depth anomalies, the large number of hotspot islands, and the slow seismic velocities, this model cannot account for the negative geoid anomaly. An uplifted lithospheric plate compensated by thermally expanded rock at depth produces a geoid high. The negative geoid signal from the compensating mass is smaller than the geoid high created by surface uplift, creating a net positive geoid anomaly. Thus, the observed negative geoid anomalies are not consistent

with a thinned lithosphere [*McNutt and Judge*, 1990]. In addition, recent determination of effective elastic plate thickness in the Marquesas and Society Island chains indicates that the thickness of the thermal lithosphere is closer to 125 km than 75 km [*Filmer et al.*, 1993].

McNutt and Judge [1990] noted that the Superswell is characterized by a negative geoid/topography admittance at wavelengths between 2500 and 5000 km. The presence of a low viscosity layer at the base of the lithosphere can produce such an admittance. If hotter than average mantle underlies the lithosphere, buoyancy stresses cause uplift of the surface. A low viscosity layer attenuates this upward force, creating an uplift smaller than if the low viscosity layer was not present. The negative geoid signal from the hot (lower density) material in the upper mantle outweighs the positive geoid signal from the surface uplift and creates a net geoid low [*Richards and Hager*, 1984]. *McNutt and Judge* [1990] compared geoid and topography response functions for different viscosity structures and found that negative admittances can occur if a layer of decreased viscosity at least several hundred kilometers thick lies at the base of the lithosphere and coincides with a region of elevated temperature. While this model is consistent with the observations, comparison of response functions alone cannot yield strong constraints on the viscosity structure.

Better estimates of radial viscosity structure can be achieved by comparing observed geoid and topography to that predicted by different viscosity models. These calculations require an additional piece of information: estimates of mantle temperature or density anomalies. Thermodynamic equations using laboratory-derived constants provide a theoretical scaling relationship between seismic velocity and density. Thus, seismic velocity models provide first-order estimates of density anomalies within the mantle. With an *a priori* knowledge of density variations and an assumed model of mantle rheology, the convectively-maintained geoid and dynamic topography can be predicted numerically. Comparisons of these predicted fields to those observed yield

plausible viscosity structures. Several global viscosity models have been suggested based on this type of analysis [*Hager and Clayton*, 1989; *Hager and Richards*, 1989; *Forte and Peltier*, 1991; *King and Masters*, 1992; *Forte et al.*, 1993; *King*, 1993; *Cazenave and Thoraval*, 1994]. The preferred viscosity profiles from these studies are shown in Figure 1.1. The solutions exhibit some similar characteristics, such as a nearly constant viscosity lower mantle at least 10 times more viscous than the upper mantle. Each of these models contains a viscosity jump at 400 km depth, the top of the transition zone. Some models have a low viscosity zone just above the transition zone (HR, HCW4, CT, K2), and other models exhibit a low viscosity layer within the transition zone itself (MODSH, MDLSH, SH425, K1). All of these models correctly predict a positive topography anomaly in the region of the Superswell, but the sign and pattern of the predicted geoid varies between models (Figure 1.2). Models K1, K2, and MODSH produce a positive geoid over the Superswell, where a negative geoid is observed. Models MDLSH and SH425 produce a negative geoid, but with very little amplitude (approximately 1 meter). Only models HR, HCW4, and CT, which all have a distinct low viscosity zone between 100 and 400 km depth produce negative geoid and positive topography anomalies of comparable magnitude to those observed. They do not completely match the observed data, however. The patterns of the predicted fields only adequately match those observed.

It is not surprising that these global viscosity models do not provide an acceptable fit to the geoid and topography data in the South Pacific. These models were derived using global geoid data at wavelengths of greater than 5000 km. We wish to explain geoid and topography observations at wavelengths of 3000-5000 km beneath the South Pacific. The goal of this study is to determine a viscosity profile which is consistent with the anomalous observations of the Superswell. What is not determined from this forward modeling exercise, however, is whether minor variants of one or more of these global models would provide an acceptable fit to the Superswell data.

The relationship between viscosity structure and the surface geoid and topography is non-unique, increasing the difficulty of determining an appropriate viscosity structure. Most previous studies have relied on forward modeling techniques. A drawback to forward modeling is that only a finite number of viscosity models can be evaluated. It is likely that only models which fit the prevailing wisdom will be tested, and models which are very different which may be equally viable will be overlooked. An alternative is to use inverse techniques. The models which are tested during the inversion are determined by the mathematics of the problem, reducing the effect of human bias on the outcome. However, the inversion must be carefully parameterized to insure that it searches a large region of the solution space so that an accurate global solution is found, not a local solution.

King and Masters [1992] inverted spherical harmonic coefficients of the geoid to invert for 11 layers of constant viscosity. Their inversion resulted in viscosity models different from those suggested previously by forward-modeling studies. Most forward modeling studies suggested viscosity structures with a low viscosity layer above the transition zone, while the viscosity models suggested by *King and Masters* [1992] indicate a low viscosity layer within the transition zone (Figure 1.1).

In this study, we formulate an inverse procedure to constrain the viscosity structure in the upper mantle within a limited geographic region. Since this is a regional study, we cannot invert for spherical harmonic coefficients of geoid and topography; we must formulate the problem in spatial coordinates. We take previously-determined viscosity models as representative of average viscosity structures and search for variations of these models which better satisfy the regional data. This technique is applied to the South Pacific Superswell, where the topographic swell and the geoid low tightly constrain the viscosity of the upper mantle.

Figure Captions

Figure 1.1. Globally representative viscosity profiles which serve as reference models in our inversion. All of these models have been determined using long-wavelength ($l \leq 8$) global geoid data. a) model W4 from *Hager and Clayton* [1989]; b) preferred viscosity model from *Cazenave and Thoraval* [1994]; c) preferred model of *Hager and Richards* [1989]; d,e) two suggested models from *King* [1993]; f,g,h) three viscosity models from *King and Masters* [1992], determined using different seismic velocity models; i,j,k) models SS1, SS2, and SS3 determined from forward modeling of geoid and topography data of the Superswell [*McNutt and Evans*, 1993].

Figure 1.2. Predicted and observed topography (top) and geoid (bottom) for two reference viscosity models. Grayscale indicates observed data and contours represent predicted data. Solid contours represent positive values, dashed contours represent negative values, and the thick solid line indicates the zero contour. Black squares mark the locations where the predicted fields are calculated. The dark gray region in the left side of the geoid map represents the region where seafloor age, and therefore the geoid anomaly is not constrained. a) Predicted data for reference model HCW4 [*Hager and Clayton*, 1989]. The pattern of topographic high and geoid low roughly coincide with the patterns in the observed data, suggesting that a variation of this model may be successful in fitting the data. b) Predicted data for reference model K1 [*King*, 1993]. Although the pattern of the observed topography is generally matched, this model predicts a geoid signal of the opposite sign than that observed.

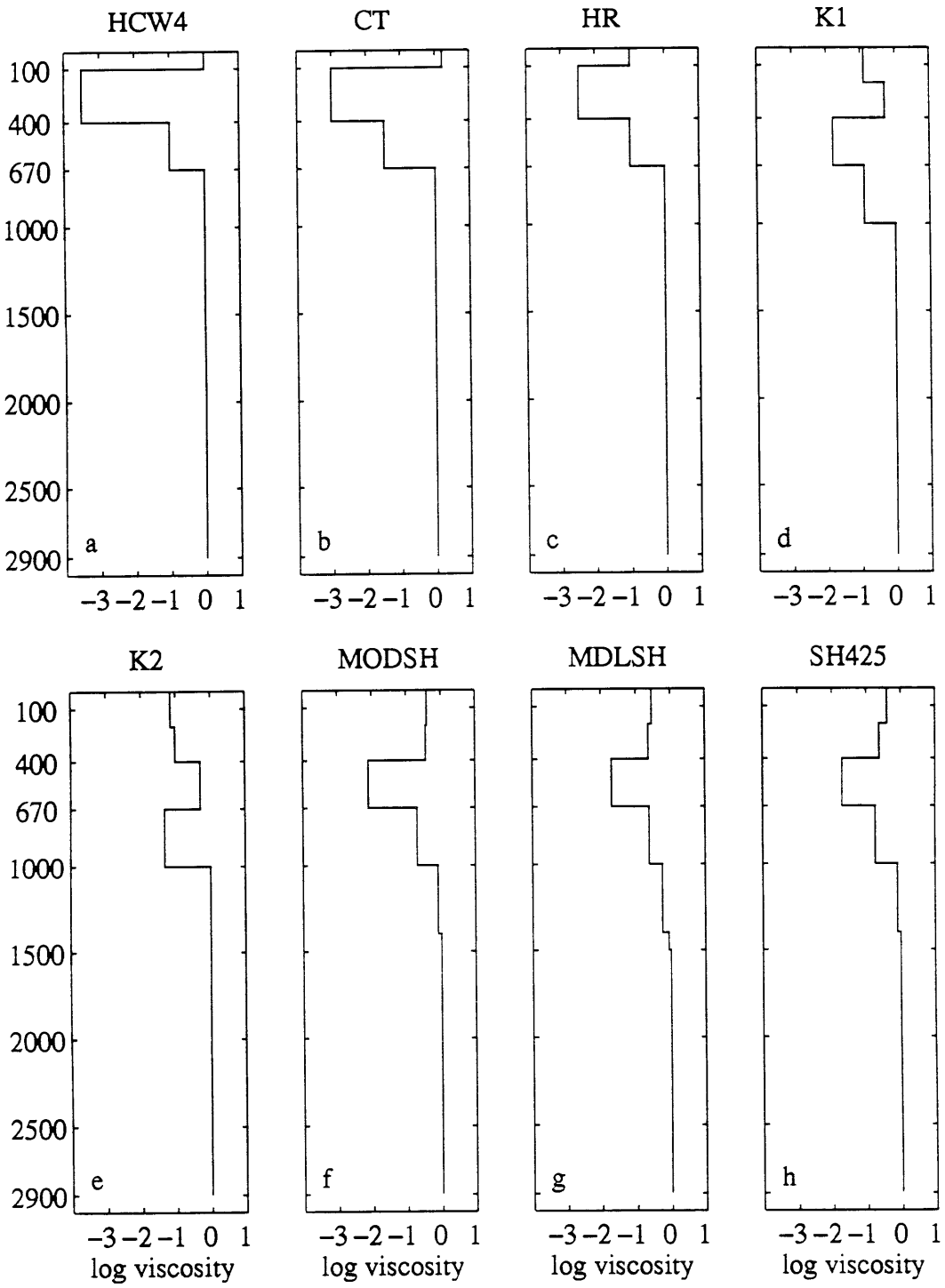
HCW4
CT
HR
K1
K2
MODSH
MDLSH
SH425
100
400
670
1000
1500
2000
2500
2900
a
b
c
d
e
f
g
h
−3 −2 −1 0 1
log viscosity

Figure 1.1

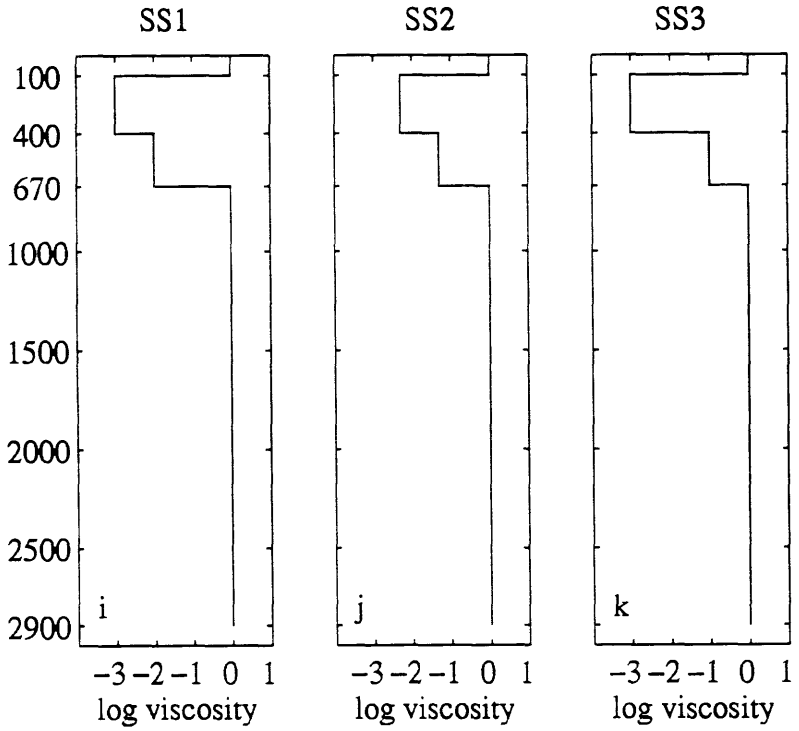

Figure 1.1 (cont.)

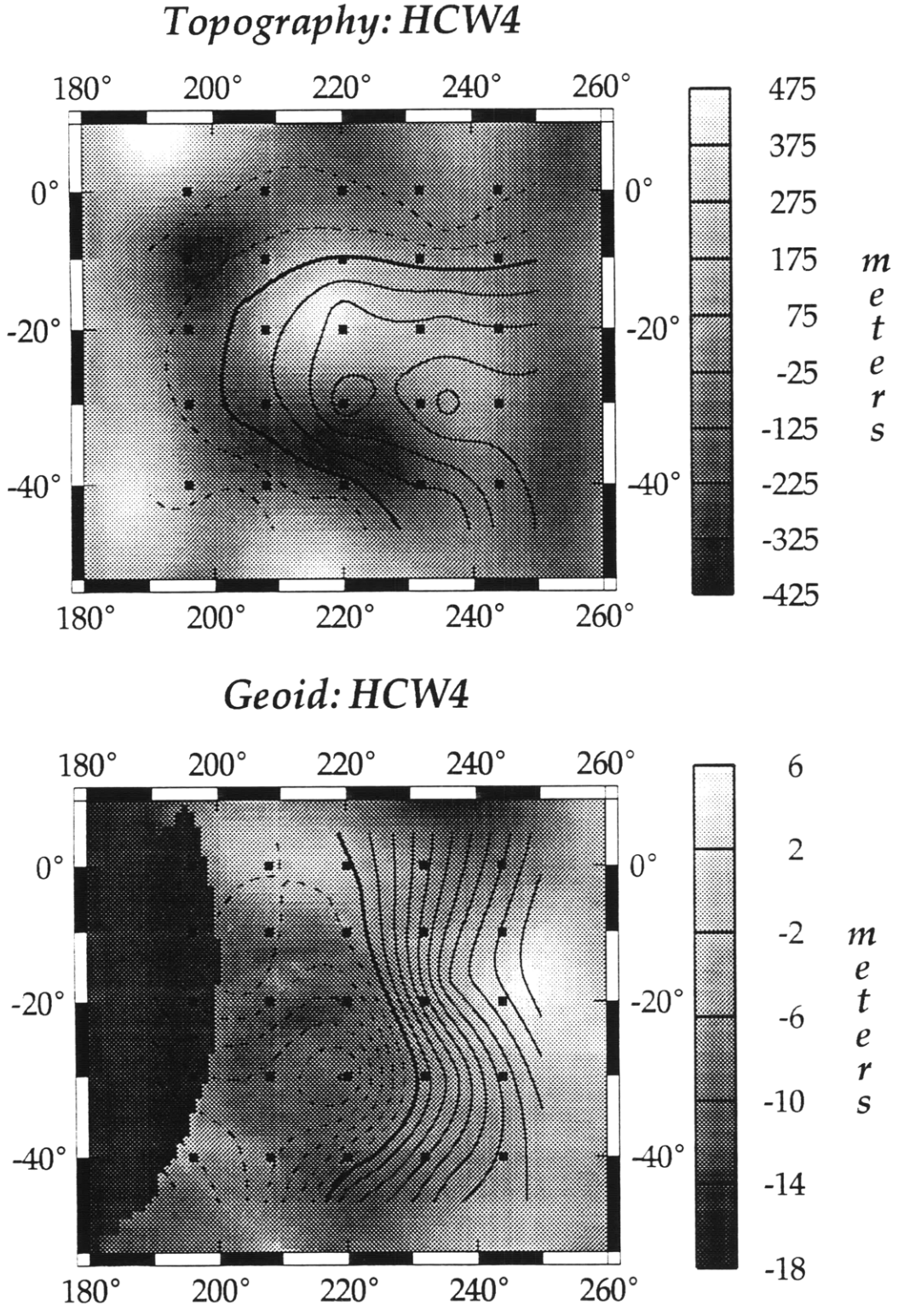
Topography: HCW4
180°
200°
220°
240°
260°
0°
-20°
-40°
475
375
275
175
75
-25
-125
-225
-325
-425
meters
Geoid: HCW4
6
2
-2
-6
-10
-14
-18

Figure 1.2a

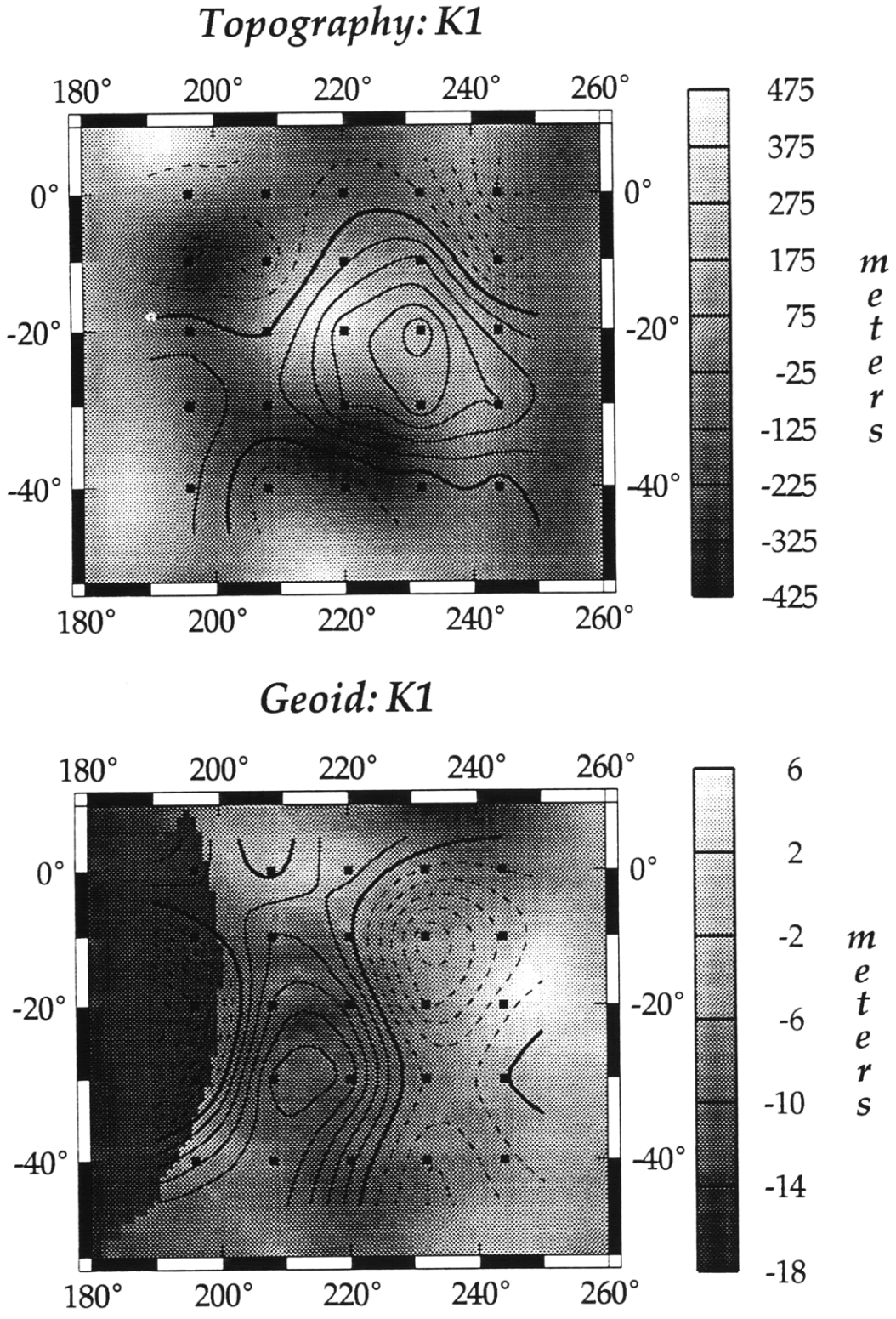
Topography: K1
180°
200°
220°
240°
260°
0°
-20°
-40°
475
375
275
175
75
-25
-125
-225
-325
-425
meters
Geoid: K1
6
2
-2
-6
-10
-14
-18

Figure 1.2b

Chapter 2: Methods

2.1 Relating Viscosity To Surface Observables: The Forward Problem

Both dynamic topography and the geoid evince internal forces. Since the geoid is a gravitational equipotential, it contains information about internal density structure of the Earth. If we consider convection within a spherical shell, the theoretical geoid anomaly is the sum of the effects from internal density variations and the induced deformations of the top and bottom boundaries. The relationship between density and the geoid is not straightforward, however. The magnitude and even the sign of the theoretical geoid anomaly strongly depends on the variations in viscosity. Thus, the observed patterns in dynamic topography and the geoid place constraints on viscosity in the mantle.

On convective time scales, the mantle behaves as a viscous fluid. We characterize the mantle as an incompressible Newtonian fluid with a radially-varying viscosity. We assume that seismic velocity models provide first-order estimates of the lateral density contrasts within the mantle which drive convection. Surface deformations are calculated by simultaneously solving the Stokes equation of motion, the continuity equation, and the constitutive relation for a Newtonian fluid:

$$-\nabla p + \eta \nabla^2 \mathbf{u} + \rho \nabla U = 0 \tag{2.1}$$

$$\nabla \cdot \mathbf{u} = 0 \tag{2.2}$$

$$\sigma = -p\mathbf{I} + 2\eta\dot{\varepsilon} \tag{2.3}$$

p is pressure, η is viscosity, $\mathbf{u}$ is the velocity vector, ρ is density, U is the gravitational potential, σ and $\dot{\varepsilon}$ are the stress and strain rate tensors and $\mathbf{I}$ is the identity matrix [*Hager and O'Connell*, 1981; *Hager and Richards*, 1989].

Since the mantle is a spherical shell, it is convenient to cast the problem in spherical coordinates and expand the velocity and stress in terms of spherical harmonic functions. Both poloidal and toroidal terms are required to fully represent velocity and stress fields. However, coupling of poloidal and toroidal fields only occurs in the presence of lateral variations in viscosity [*Hager and Clayton*, 1989], which we assume are negligible, therefore we ignore poloidal terms in our analysis. The toroidal terms of the velocity field and stress tensor are given by:

$$\mathbf{u}(r,\theta,\phi) = y_1^{lm} Y_{lm}(\theta,\phi)\,\hat{\mathbf{r}} + y_2^{lm}\left[Y_{lm}^{\theta}(\theta,\phi)\,\hat{\theta} + Y_{lm}^{\phi}(\theta,\phi)\,\hat{\phi}\right] \tag{2.4}$$

$$\sigma(r,\theta,\phi) = \sigma_{rr}^{lm} Y_{lm}(\theta,\phi)\,\hat{\mathbf{r}} + \sigma_{r\theta}^{lm}\left[Y_{lm}^{\theta}(\theta,\phi)\,\hat{\theta} + Y_{lm}^{\phi}(\theta,\phi)\,\hat{\phi}\right] \tag{2.5}$$

$Y_{lm}(\theta,\phi)$ is a spherical harmonic function of degree l and order m defined in terms of colatitude θ and longitude ϕ:

$$Y_{lm}(\theta,\phi) = P_{lm}(\cos\theta)\begin{cases}\sin m\phi, & -l \le m < 0\\ \cos m\phi, & 0 \le m \le l\end{cases} \tag{2.6}$$

Its derivatives are abbreviated

$$Y_{lm}^{\theta} = \frac{\partial Y_{lm}}{\partial\,\theta} \qquad \text{and} \qquad Y_{lm}^{\phi} = \frac{1}{\sin\theta}\frac{\partial Y_{lm}}{\partial\,\phi} \tag{2.7}$$

[*Hager and Clayton*, 1989]. When the three governing equations (2.1-2.3) are written in spherical coordinates and terms are separated by degree and order, they can be transformed to a 6 by 6 system of differential equations of the form:

$$\frac{\partial \mathbf{y}}{\partial r} = \frac{1}{r}\mathbf{A}\mathbf{y} \tag{2.8}$$

where the vector $\mathbf{y}$ contains radially dependent coefficients of the velocities, stresses, and the gravitational potential. This system may be simplified by defining an effective radial

stress $\tilde{\sigma}_{rr}^{lm} = \sigma_{rr}^{lm} + \rho U_{lm}$ and solving for the potential coefficients separately. The solutions for the velocity and stress then become decoupled from the solutions for the potential and equation (2.8) is reduced to a 4 by 4 system in which:

$$\mathbf{y} = [y_1^{lm}, y_2^{lm}, r\tilde{\sigma}_{rr}^{lm}, r\sigma_{r\theta}^{lm}]^T \tag{2.9}$$

and

$$\mathbf{A} = \begin{bmatrix} -2 & l(l+1) & 0 & 0 \\ -1 & 1 & 0 & 1/\eta \\ 12\eta & -6l(l+1)\eta & 1 & l(l+1) \\ -6\eta & 2[2l(l+1)-1]\eta & -1 & -2 \end{bmatrix} \tag{2.10}$$

[*Judge*, 1986; *Hager and Clayton*, 1989]. Note that the A_{24} term, relating the radial derivative of tangential velocity to tangential stress is $1/\eta$, making this system of equations non-linear in viscosity. To simplify calculations, variables are non-dimensionalized as follows:

$$u_{lm} = \frac{\rho_o g \alpha T_o a^2}{\eta_o} u'_{lm} \qquad \sigma_{lm} = \rho_o g \alpha T_o a \, \sigma'_{lm} \tag{2.11}$$

$$r = ar' \qquad \eta = \eta_o \eta'$$

where ρ_o is the density at the reference temperature T_o, α is the coefficient of thermal expansion, a is the radius of the Earth, η_o is a reference viscosity and g is the average gravitational acceleration at the surface [*Judge*, 1986]. In subsequent equations, primes are dropped for notational convenience and variables are considered non-dimensional unless otherwise specified. Green's function solutions are found by introducing a unit density anomaly at a radius r. At this point, radial and tangential velocities and shear stress are continuous, but the radial stress exhibits a jump due to the density perturbation. These boundary conditions as well as free-slip conditions at the surface and the CMB are applied and equation (2.8) is solved analytically through the use of propagator matrices [*Hager and Clayton*, 1989]. Expressions for the surface and CMB deformations are derived by expanding the stresses at the surface and the CMB in a Taylor series and matching the stresses across the boundaries. By calculating the predicted boundary

deformation as a function of the radius of the density anomaly, we obtain response functions of the surface and CMB deformations, $H_s^l(r)$ and $H_b^l(r)$. These response functions, or kernels, characterize the amount of boundary deflection due to a unit density anomaly of degree l at radius r. Examples of these kernels for two different viscosity structures are shown in Figure 2.1. The integrated product of the kernels and the non-dimensionalized density structure yields spherical harmonic coefficients for the surface topography and the geoid:

$$h_{lm} = \frac{\rho_o}{(\rho_o - \rho_w)} \int_{r_c}^{1} H_s^l(r, \eta(r))\, \delta\rho_{lm}(r)\, dr \tag{2.12}$$

$$N_{lm} = \frac{4\pi G a^2}{2l+1} \int_{r_c}^{1} G^l(r, \eta(r))\, \delta\rho_{lm}(r)\, dr \tag{2.13}$$

where

$$G^l(r) = H_s^l(r) - r^{l+2} + r_c^{l+2} H_b^l(r) \tag{2.14}$$

If we assume that density anomalies are linearly related to the seismic anomalies, then

$$\delta\rho_{lm}(r) = -\frac{\partial \ln\rho}{\partial \ln v_s}\, \delta v_{lm}^s(r) \tag{2.15}$$

where $\delta v_{lm}^s(r)$ is a non-dimensional shear velocity anomaly. $\partial \ln\rho / \partial \ln v_s$ is the density-velocity scaling relation which we take to be a constant. As indicated in equation (2.14), the geoid kernel, $G^l(r)$, contains the effects of the surface boundary deformation, the driving density anomaly, and the core-mantle boundary deformation on the surface geoid. These kernels are functions only of the boundary conditions and relative viscosity variations throughout the mantle; they are not dependent on the absolute viscosity.

Since we perform a regional study, we cannot compare the observed and predicted geoid and topography in the spectral domain; the comparison must be made in the spatial domain. Therefore, we expand the spherical harmonic coefficients for geoid and topography given in (2.12-2.13)

$$\left.\begin{matrix} N(\theta,\phi) \\ h(\theta,\phi) \end{matrix}\right\} = \sum_{l=0}^{\infty} \sum_{m=-l}^{l} \left\{ \begin{matrix} N_{lm}(\eta(r)) \\ h_{lm}(\eta(r)) \end{matrix} \right\} Y_{lm}(\theta,\phi) \tag{2.16}$$

to obtain predicted geoid and topography values in the spatial domain. To prevent aliasing, we limit the expansion to harmonic degrees corresponding to wavelengths smaller than the greatest dimension of the region. The expansion is also limited at the short wavelengths by the resolution of the seismic velocity data. For the case of the Superswell, this limits the expansion in (2.16) to l = 8-12.

2.2 Formulation of the Inverse Problem

The relationship between viscosity structure and geoid and topography is non-unique. Theoretically, there exist an infinite number of solutions which predict the same surface observables. Fortunately, not all mathematically feasible solutions make sense physically. Some solutions may exhibit a large amount of detailed structure, such as large oscillations in viscosity with depth, which are difficult to reconcile with our seismological and mineralogical understanding of the mantle. In addition, detailed viscosity models invite over-interpretation of the data. Since we do not have the resolving power to accurately determine a complex viscosity structure, it is sensible to select the simplest solution which satisfies the data. In formulating the inverse problem, we have chosen to determine a viscosity model which satisfies the data, yet is closest to a globally representative viscosity profile. This added constraint provides us with solutions which are consistent with our global knowledge of mantle structure, yet allow for significant variation to yield a viscosity profile which satisfies the data for the region of interest.

We determine a viscosity structure which minimizes the rms misfit of the model predictions to the data, subject to an outside constraint. A common constraint is the requirement that the model be smooth [*Constable et al.*, 1987]. However, smoothness is not necessarily a desired quality for radial viscosity. Seismic studies indicate density

discontinuities at 400 km and 670 km depth within the upper mantle. These discontinuities are believed to be phase changes of mantle minerals induced by temperature and pressure. Since sharp changes in seismic velocity and density are observed, these discontinuities are likely to be accompanied by rather sharp changes in viscosity. Rather than searching for the smoothest possible viscosity model, we choose the constraint that our solution be as close as possible to previously determined global viscosity model.

We follow *Constable et al.* [1987] in our methods and represent viscosity as a model vector $\mathbf{m}$ of length N. The data vector, $\mathbf{d}$, consists of geoid and topography observations at a series of M observation points, $\mathbf{d} = \left[N_1, \cdots, N_M, h_1, \cdots, h_M\right]^T$. These vectors are related via a nonlinear forward functional $\mathbf{d} = \mathbf{F}[\mathbf{m}]$, given in (2.16). In our inversions, we seek the viscosity solution $\mathbf{m}$ subject to the constraints that the misfit of the model predictions to the data, χ^2, is within an acceptable tolerance and that $\mathbf{m}$ is a close as possible to an assumed viscosity profile $\mathbf{m}^*$, such as those derived from global analyses. The misfit of the model predictions to the data is given by

$$\chi^2 = \left\| \mathbf{Wd} - \mathbf{WF}[\mathbf{m}] \right\|^2 \tag{2.17}$$

$\mathbf{W}$ is a diagonal weighting matrix whose elements are the inverse of the uncertainties associated with each measurement, $\mathbf{W} = \mathrm{diag}\left\{ 1/\sigma_1, 1/\sigma_2, \cdots, 1/\sigma_{2M} \right\}$. We wish to minimize this misfit subject to the constraint that our model $\mathbf{m}$ be as close as possible to an *a priori* model $\mathbf{m}^*$. The constraint, $\left\| \mathbf{m} - \mathbf{m}^* \right\|^2$, is multiplied by a Lagrange multiplier and added to the quantity to be minimized, χ^2. This new functional, U, is stationary where the derivative of the functional is zero. If μ^{-1} is the Lagrange multiplier the new functional becomes:

$$U = \left\| \mathbf{m} - \mathbf{m}^* \right\|^2 + \mu^{-1} \left\{ \left\| \mathbf{Wd} - \mathbf{WF}[\mathbf{m}] \right\|^2 \right\} \tag{2.18}$$

Inspection of equation (2.18) shows that the functional U contains the two quantities to be minimized. The first term represents the constraint that the solution be close to a

reference model. The term within the brackets represents the rms misfit of the model to the data. We set $\nabla_m U = 0$ to find the stationary point, this yields the solution vector $\mathbf{m}$. For a linear forward functional, the solution becomes:

$$\mathbf{m} = \left[(\mathbf{WJ})^T \mathbf{WJ} + \mu\right]^{-1} \left(\mu \mathbf{m}^* + (\mathbf{WJ})^T \mathbf{Wd}\right) \tag{2.19}$$

where $\mathbf{J}$ is the Jacobian, given by

$$J_{ij} = \frac{\partial F_i[\mathbf{m}]}{\partial m_j} \tag{2.20}$$

Since the relationship between the model viscosity and the data is non-linear, the Jacobian $\mathbf{J}$ depends upon the solution vector $\mathbf{m}$ and a direct solution of the problem is not possible. Instead, we linearize the problem, solve for an approximate solution, and iterate until a satisfactory solution is found. We assume that the functional $\mathbf{F}$ is differentiable, and therefore

$$\mathbf{F}[\Delta] = \mathbf{F}[\mathbf{m}_1] + \mathbf{J}_1[\Delta] \tag{2.21}$$

to first order, for sufficiently small vectors $\Delta = \mathbf{m}_2 - \mathbf{m}_1$. $\mathbf{J}_1$ denotes the Jacobian evaluated for model $\mathbf{m}_1$. Substituting this approximation into equation (2.18), we obtain

$$U = \left\| \mathbf{m}_2 - \mathbf{m}^* \right\|^2 + \mu^{-1} \left\{ \left\| \mathbf{W}\left(\mathbf{d} - \mathbf{F}[\mathbf{m}_1] + \mathbf{J}_1 \mathbf{m}_1\right) - \mathbf{WJ}_1 \mathbf{m}_2 \right\|^2 \right\} \tag{2.22}$$

If we define the term in parenthesis as $\hat{\mathbf{d}}_1$, then (2.22) becomes analogous to (2.18). Again $\nabla_m U$ is set to zero and we obtain the solution vector $\mathbf{m}_2$:

$$\mathbf{m}_2 = \left[(\mathbf{WJ}_1)^T \mathbf{WJ}_1 + \mu\right]^{-1} \left(\mu \mathbf{m}^* + (\mathbf{WJ}_1)^T \mathbf{W}\hat{\mathbf{d}}_1\right) \tag{2.23}$$

μ is still a free parameter in this equation. The value of μ determines the trade-off between how well $\mathbf{m}_2$ satisfies the data and how much it differs from $\mathbf{m}^*$. Inspection of (2.22) indicates that if μ is large, then the data misfit term becomes small and $\mathbf{m}_2$ is close to $\mathbf{m}^*$. Conversely, if μ is small, $\mathbf{m}_2$ satisfies the data well, but can vary substantially from $\mathbf{m}^*$. We wish to find the minimum perturbation of $\mathbf{m}^*$ sufficient to satisfy the data. To do so, we generalize (2.23) to form an iterative scheme.

$$\mathbf{m}_{k+1} = \left[(\mathbf{W}\mathbf{J}_k)^T \mathbf{W}\mathbf{J}_k + \mu \right]^{-1} \left(\mu \mathbf{m}^* + (\mathbf{W}\mathbf{J}_k)^T \mathbf{W}\hat{\mathbf{d}}_k \right) \tag{2.24}$$

For a fixed value of μ, we calculate a solution, $\mathbf{m}_{k+1}$; this solution becomes the starting model for the subsequent iteration. Iteration continues until the misfit reaches a minimum. We then increment μ and repeat the process, obtaining a series of solutions for different values of μ. The solution corresponding to the largest μ (closest to the reference model $\mathbf{m}^*$) which has an rms misfit within an acceptable tolerance, is our preferred solution (Figure 2.2).

A limitation of the current formulation of the inversion is that the prediction of data (2.12-2.13) involves only six terms, one corresponding to each layer of viscosity. The geoid and topography kernels vary rapidly with radius for degrees 8-12 and viscosity structures with large contrasts in viscosity (Figure 2.1b). The kernels are sampled only three times in the uppermost mantle where they are highly variable. Thus it is difficult to determine the depth and the magnitude of the geoid kernel peak and the depth of the rapid fall-off of the topography kernel, which are very sensitive to the depth and magnitude of viscosity contrasts. Therefore, much of the detail of the kernels, as well as the radial variation in seismic velocity is lost. This makes it difficult to determine the difference in predicted data between viscosity profiles which contain large contrasts in viscosity between layers. Methods to remedy this situation are discussed in Chapter 5.

Figure Captions

Figure 2.1. Normalized response functions for surface topography, core-mantle boundary deformation and the geoid for two radial viscosity profiles. Kernels for three harmonics are shown: degree 8 (solid line), degree 10 (dashed line), and degree 12 (dot-dash line). a) model HCW4; b) model MODSH. The depth and magnitude of a low viscosity layer produces much larger differences in the geoid kernels than in the topography kernels. This indicates that geoid observations place a tighter constraint than topography data on acceptable viscosity models.

Figure 2.2. Schematic illustration of best-fit viscosity solution. The best solution corresponds to the largest value of μ for which χ^2 is a minimum. This provides a solution which is closest to the reference model, $\mathbf{m}^*$, yet satisfies the data.

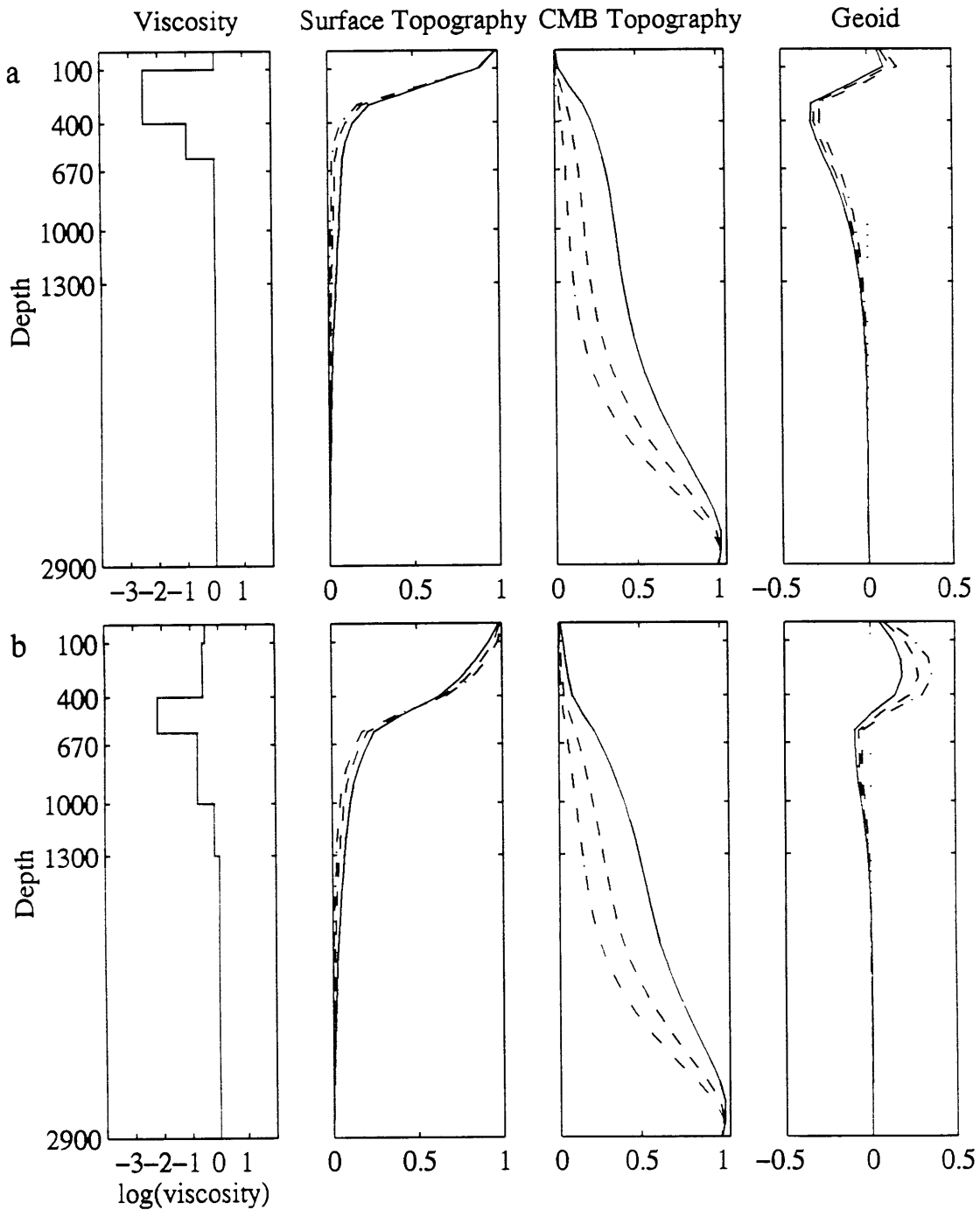
Viscosity
Surface Topography
CMB Topography
Geoid
a
b
Depth
100
400
670
1000
1300
2900
−3 −2 −1 0 1
0 0.5 1
−0.5 0 0.5
log(viscosity)

Figure 2.1

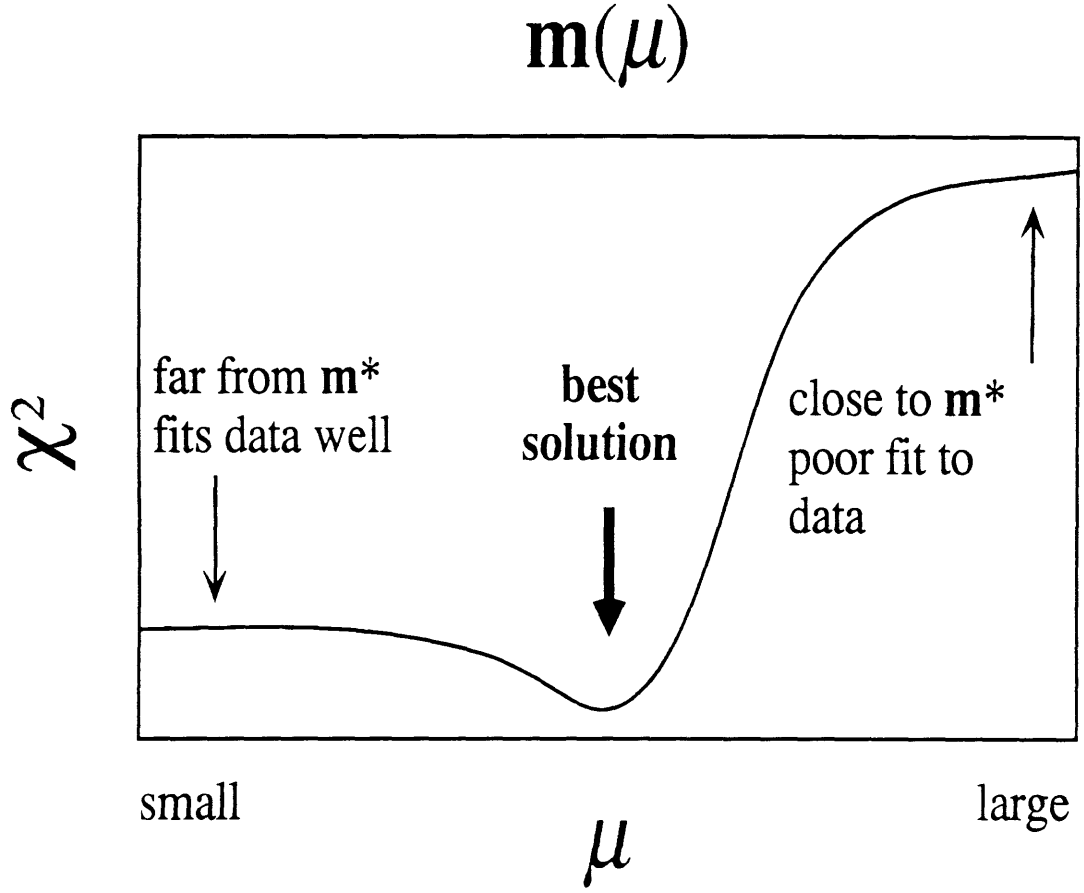
m(μ)
χ²
far from m*
fits data well
best
solution
close to m*
poor fit to
data
small
μ
large

Figure 2.2

Chapter 3: Data

3.1 Topography

A successful viscosity model must be consistent with the observed dynamic topography. Oceanic topography has two major components: short-wavelength topography which is compensated by variations in crustal thickness, elastic plate flexure, and long-wavelength dynamic topography which is compensated by density anomalies below the lithosphere. We isolate the dynamic component of topography by removing the effects of two sources of crustal thickness variations: seafloor cooling and hotspot volcanism. Bathymetry is obtained on a 5 arc-minute grid from the ETOPO-5 topographic database [*National Geophysical Data Center*, 1988] (Figure 3.1a). The component of topography due to seafloor cooling is removed by subtracting the depth which the seafloor has subsided since it was formed at the mid-ocean ridge. *Müller et al.* [1993] have compiled a digital grid of seafloor age data (Figure 3.2) based on a self-consistent set of isochrons determined from magnetic lineations, plate tectonic reconstructions, and fracture zones. Once the age of the lithosphere is known, the estimated amount of seafloor subsidence (in meters) can be calculated from the empirical relationship determined by *Parsons and Sclater* [1977]:

$$d(t) = \begin{cases} 2500 + 350\sqrt{t} & 0 < t < 70\text{Ma} \\ 6400 - 3200e^{-t/62.8} & t > 70\text{Ma} \end{cases} \tag{3.1}$$

The difference between the ETOPO-5 bathymetry and the predicted subsidence is the depth anomaly, and represents the topography of the ocean floor relative to

"normal" oceanic lithosphere. Figure 3.1 illustrates the observed topography of French Polynesia and the depth anomaly after the effect of seafloor cooling has been removed. The most apparent features are the large number of islands and seamounts in this region due to mid-plate volcanism. A broad topographic swell is also apparent in the topography, but even more evident in the topography anomaly. Since lithospheric age increases to the west, the depth of the seafloor should gradually deepen due to lithospheric cooling. Instead, the depth gradually increases, increasing the discrepancy between the observed bathymetry and predicted depths, resulting in a distinct positive depth anomaly which can be seen in Figure 3.1c.

Most of the short wavelength topography which remains is a result of mid-plate volcanism. This volcanic topography must be separated from the dynamic component of the topography. Volcanic edifices are compensated by a crustal root, causing a downwarping of the crust-mantle boundary, the Moho. Dynamic topography, however, is compensated by hot, low-density material beneath the lithosphere, resulting in an upward deflection of the Moho. Since the crust-mantle boundary is an intrinsic density interface, geoid observations can distinguish whether positive topography is accompanied by a positive or negative deflection of the Moho. We use a linear filtering technique developed by *McNutt and Shure* [1986] to separate the components of topography which are compensated within the lithosphere and below the lithosphere.

If the lithosphere behaves as a thin elastic plate, then it is straightforward to predict the surface topography and geoid resulting from either crustal thickness variations or sub-surface loading. The observed geoid and topography are the sum of the two effects. The fact that these two phenomena deflect the Moho in opposite directions can be used to separate short-wavelength island topography from long-wavelength dynamic topography. It can be shown (see *McNutt and Shure* [1986] for derivation) that the predicted swell topography is given by :

$$W_l(k_x,k_y)=\frac{gk}{G}\left\{\left[\frac{\rho_o-\rho_w}{1+k^4\alpha}+(\rho_m-\rho_o)\right]e^{-2\pi kz_m}\right.$$
$$\left.-\left[(\rho_o-\rho_w)+(\rho_m-\rho_o)k^4\alpha\right]e^{-2\pi kz_l}\right\}^{-1} N_R(k_x,k_y) \qquad (3.2)$$

$$N_R(k_x,k_y)=N-\frac{G(\rho_o-\rho_w)}{gk}\left\{e^{-2\pi kz_l}-\frac{e^{-2\pi kz_m}}{1+k^4\alpha}\right\}H(k_x,k_y)$$

where α is the flexural parameter; k_x and k_y are horizontal wavenumbers, $k=\sqrt{k_x^2+k_y^2}$; ρ_o, ρ_w, ρ_m are densities of the volcanic rock, water, and mantle; G is the universal gravitational constant; g is gravitational acceleration; z_l and z_m are the average depth of topography and the Moho; and H, N, and W_l are the Fourier transforms of the topography, geoid, and swell topography. N_R is the reduced geoid anomaly, N-$\hat{N}$, where $\hat{N}$ is the geoid predicted if one incorrectly assumes that all topography is due to thickening of the crustal layer.

Figure 3.3 shows such a separation of topography for the Society Islands. The short wavelength topography due to the islands (Figure 3.3b) has been isolated from the longer wavelength topography due to sub-lithospheric forces (Figure 3.3c). Note that the gradual increase in topography surrounding the islands which is apparent in the topography anomaly is not present in the island topography; the seafloor surrounding the islands in Figure 3.3b is virtually flat. This indicates that the swell topography has been accurately removed. We perform this calculation for four island groups within the Superswell: the Marquesas, Society, Cook-Austral, and the Tuamoto Island chains. Island signatures in the bathymetry are subtracted from the topography anomaly, providing an estimate of dynamic topography.

Since we perform a regional inversion, our data are limited spectrally to spherical harmonic degrees 8 through 12. We therefore filter the dynamic topography to wavelengths between 3300-5000 km before it is input into the inversion (Figure 3.4). Many corrections have been applied to the topography data, so it is difficult to determine the uncertainty in our estimate of dynamic topography. Based on an analysis by

Smith [1993], we adopt a nominal error of 50 m in the ETOPO-5 data in this region. We estimate that the uncertainty in the estimated dynamic topography is approximately 150 m, and this value is used in the weighting matrix **W** (2.17) for our calculation. Although there may be a high uncertainty in the magnitude of dynamic topography, the topography must exhibit a positive swell beneath these islands. This requirement that the sign of the topography be positive provides a constraint on the viscosity structure itself.

3.2 Geoid

Geoid measurements provide one set of observational constraints on an acceptable viscosity model. We obtain geoid data by combining satellite altimeter profiles from the ERS-1, Geosat, and Seasat missions [*Sandwell and Smith*, 1992]. We adopt a nominal error in the geoid of 50 cm. This is the error estimate for the geoid which we use in determining the matrix **W** (2.17).

The observed geoid field contains information about variations in density within the lithosphere and throughout the mantle. We wish to isolate the geoid component related to mantle density anomalies, so the effect of density variations within the lithosphere must be removed. The effect of seafloor cooling can be assessed by modeling the lithosphere as a moving plate undergoing conductive cooling. Since plates move perpendicular to mid-ocean ridges as they cool, the system is relatively homogeneous parallel to the mid-ocean ridge and can thus be approximated as a two-dimensional phenomenon. The geoid height, N, relative to that of the mid-ocean ridge is given by:

$$N = \frac{\alpha \rho_m T_m a^2}{4\bar{\rho} R}\left[1 - \frac{12}{\pi^2}\sum_{n-1}^{\infty}\frac{(-1)^{n+1}}{n^2}\exp\left(\frac{-\beta_n u t}{a}\right)\right] \tag{3.3}$$

with

$$\beta_n = \left[\sqrt{R^2 + n^2\pi^2} - R\right], \qquad R = \frac{ua}{2\kappa}$$

where α is the coefficient of thermal expansion, κ is the thermal diffusivity, ρ_m and T_m are the density and temperature at the base of the plate, a is the plate thickness, t is the

plate age and, u is the plate velocity [*Parsons and Richter*, 1980]. This predicted geoid is shown if Figure 3.5b. Although the sum in equation (3.3) contains an infinite number of terms, the geoid can be determined to sufficient accuracy by retaining only the first five terms.

3.3 Seismic Velocity

Seismic velocity anomalies provide estimates of density anomalies within the mantle that drive convection. We use the shear wave heterogeneity model SH12/WM13 of *Su et al.* [1994], which is determined using waveform data of long-period seismograms and *SS*-*S* and *ScS*-*S* differential travel times. The model is parameterized geographically by spherical harmonic coefficients up to degree and order 12, and radially throughout the mantle by Chebyshev polynomials to degree 13. We average the velocity anomalies to represent the mean velocity pattern within each of the radial layers in the viscosity model vector **m.** The averaged anomalies are scaled to equivalent density variations and are included in the prediction of geoid and topography (2.15).

Since we perform a regional inversion, we must limit our input data to spherical harmonic degrees 8 through 12. Unfortunately, this is at the upper limit of resolution of the seismic model. Since spectral power decreases rapidly with increasing harmonic degree, the seismic model may not be well determined at these wavelengths. Resolution tests performed by *Su et al.* [1994] indicate that the resolving power of the inversion used to generate SH12/WM13 is rather good in the upper mantle. Synthetic seismic data was calculated based on a hypothetical velocity structure containing only a single harmonic. The horizontal resolution of the velocity solution was good and 90% of the amplitude of the synthetic signal was recovered at depths less than 1300 km up to $l = 12$. The resolution at these depths depends upon the spatial distribution of *SS* and *SS*-*S* travel time residual measurements, as well as the travel paths of body waves. In the vicinity of the Superswell, there are very few *SS*-*S* bounce points, however the distribution of *SS*

absolute travel times is quite good. These data sets provide sparse sampling of the mantle above 500 km, but good sampling between 500 and 1500 km depth. However, waveform data of surface waves provide good coverage at shallow depths. Resolution tests show that horizontal resolution in the South Pacific is quite good above 500 km and below 1000 km depth, but slightly poorer at depths between 500 and 1000 km [*Su et al.*, 1994].

3.4 Data Parameterization

With the exception of density interfaces and abrupt changes in mineralogy, the viscosity within the earth's mantle is likely to vary continuously with radius. To simplify the mathematics, calculations of mantle dynamics approximate a continuous viscosity structure as a series of layers of uniform viscosity. A large number of thin layers better describes a continuously varying viscosity; however, each layer of viscosity adds another free parameter to the problem. Small changes in viscosity in adjacent layers can offset one another and produce nearly identical geoid and topography, thereby increasing the difficulty of constraining the actual viscosity profile. In an attempt to minimize this effect, we limit our model to six radial shells with boundaries at 100, 400, 670, 1000, 1300, and 2890 km depth. While the designation of these shells is somewhat arbitrary, we have placed boundaries at depths of seismically-determined density contrasts (e.g. 400 and 670 km) where viscosity is likely to exhibit large discontinuities, and at depths used in previous viscosity studies (e.g. 1000, 1300 km) to facilitate the inclusion of these viscosity models in our inversion. In addition, we have placed most of the radial shells in the upper mantle since the geoid and topography at l = 8-12 are not very sensitive to viscosity variations below 1300 km at the wavelengths of interest (3300 to 5000 km). This can easily be seen by comparing the magnitudes of the surface topography and geoid kernels below 1300 km to those in the upper mantle (Figure 2.1).

Geoid and dynamic topography are parameterized as a vector of discrete values at 25 geographical points spaced every 12° between 200° to 260° E longitude and every 10° between -50° to 5° latitude. Although this provides only a modest number of data points,

it is sufficient spacing to identify the patterns of interest in the geoid and topography fields, and the number of data (50) remain small enough to maintain the stability of the inversion. Initially, we attempted the inversion with 64 latitude, longitude points (128 data) and 15 layers of viscosity. However, this provided too many degrees of freedom and the inversion was unstable. With 50 data and 5 layers of viscosity, the inversion shows stability in tests with synthetic data.

Figure Captions

Figure 3.1. a) Observed bathymetry as determined from the ETOPO-5 data set [*National Geophysical Data Center*, 1988], 500 m contours. b) Bathymetry predicted by the seafloor cooling model of *Parsons and Sclater* [1977], using ocean floor age data of *Müller et al.* [1993], 500 m contours. c) Depth anomaly obtained by subtracting the predicted bathymetry from that observed; 500 m contours. The broad topographic high which characterizes the Superswell is evident between 200° and 220° longitude. It is more pronounced in the depth anomaly because the seafloor deepens to the west more slowly than "normal" oceanic lithosphere of the same age.

Figure 3.2. Map of seafloor age in the South Pacific from *Müller et al.* [1993]. Lithospheric age increases from approximately 10 Ma at the eastern edge of the of this region (240° longitude) to 60 Ma at the western edge (200°). The signature of seafloor cooling is substantial in both the bathymetry and the geoid and must be removed. The dark gray areas represent regions where sufficient data of seafloor age is not available. Contours are drawn at 5 Ma intervals. Triangles indicate the locations of hotspots.

Figure 3.3. Separation of the observed depth anomaly into two components for the Society Island chain: a) Observed depth anomaly, 500 m contours; b) Topography due to crustal thickness variations and elastic plate flexure, 500 m contours; c) long-wavelength portion of the topography which is supported by sub-lithospheric forces.

Figure 3.4. Grayscale represents the observed depth anomaly (Figure 3.1 c). Contours represent our estimate of dynamic topography. The observed bathymetry has been corrected for seafloor cooling, crustal thickness variations and elastic plate flexure and has been filtered to wavelengths of 3300 km - 5000 km to yield dynamic topography. Note that the region of highest topography coincides with the peak in the dynamic topography. Solid lines represent positive contours, dashed lines signify negative values, and the thick solid line indicates the zero contour; 1000 m contours. Triangles indicate the locations of hotspots.

Figure 3.5. a) Observed geoid as determined from *Sandwell and Smith* [1992], 2 m contours. b) Geoid predicted by the seafloor cooling model of [*Parsons and Richter*, 1980], using the ocean floor age data set of *Müller et al.* [1993], 2 m contours. c) Geoid anomaly obtained by subtracting the predicted geoid from that observed; 2 m contours. A geoid low occurs between 200° and 220° longitude, and coincides with the location of the topographic high (Figure 3.1). Triangles indicate the locations of hotspots.

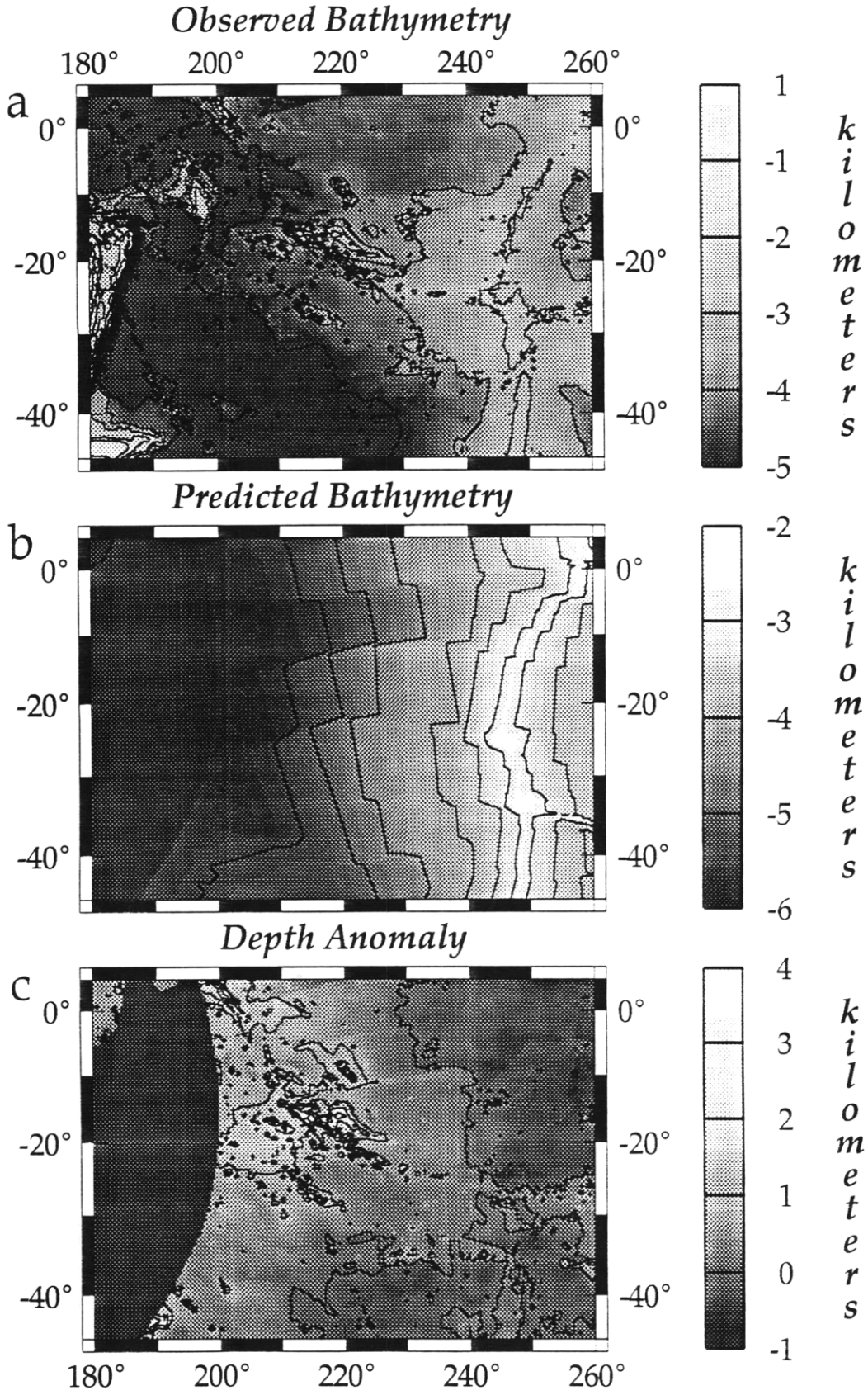
Observed Bathymetry
a
180°
200°
220°
240°
260°
0°
-20°
-40°
1
-1
-2
-3
-4
-5
kilometers
Predicted Bathymetry
b
-2
-3
-4
-5
-6
kilometers
Depth Anomaly
c
4
3
2
1
0
-1
kilometers

Figure 3.1

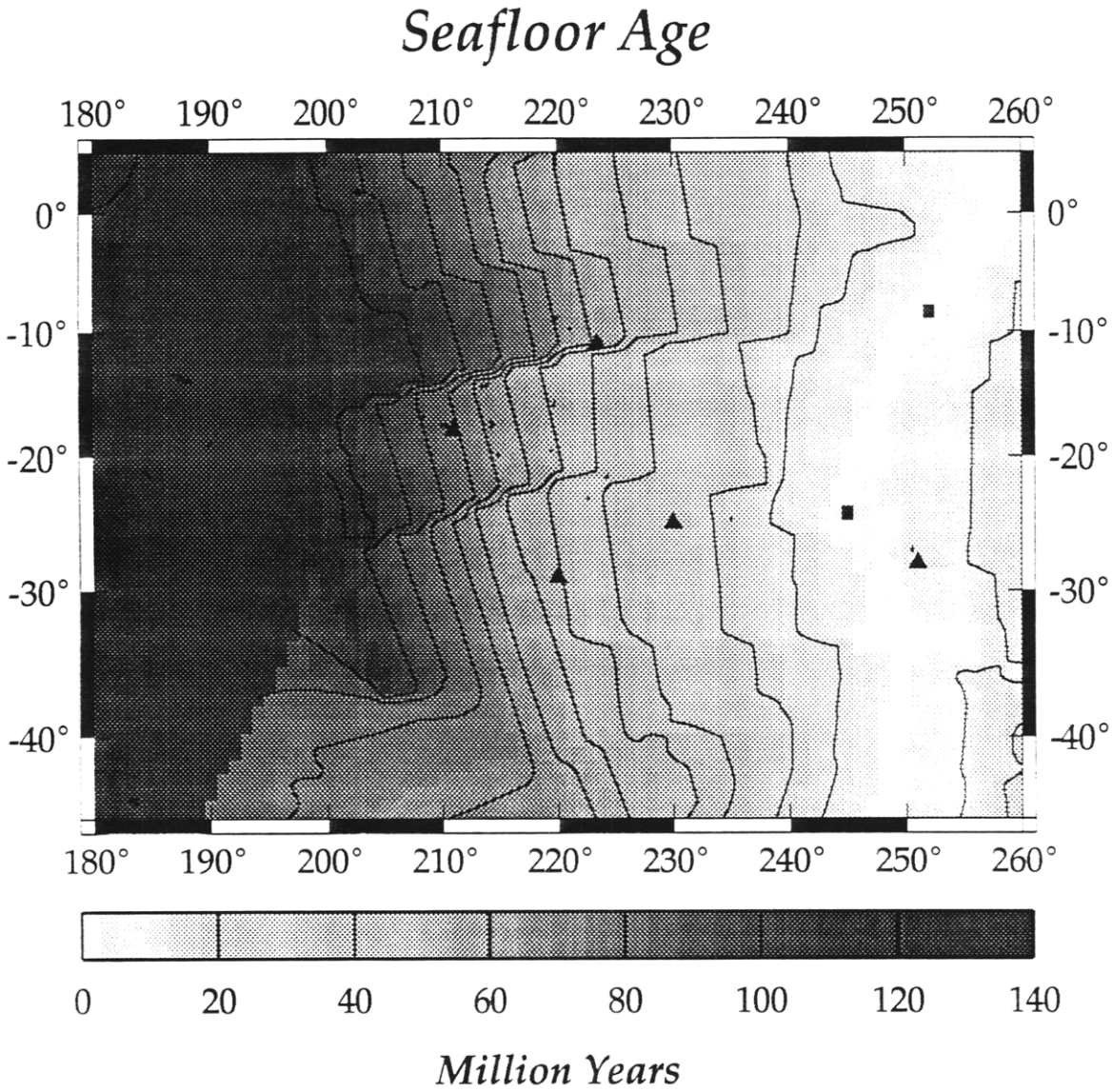
Seafloor Age
180° 190° 200° 210° 220° 230° 240° 250° 260°
0°
-10°
-20°
-30°
-40°
0 20 40 60 80 100 120 140
Million Years

Figure 3.2

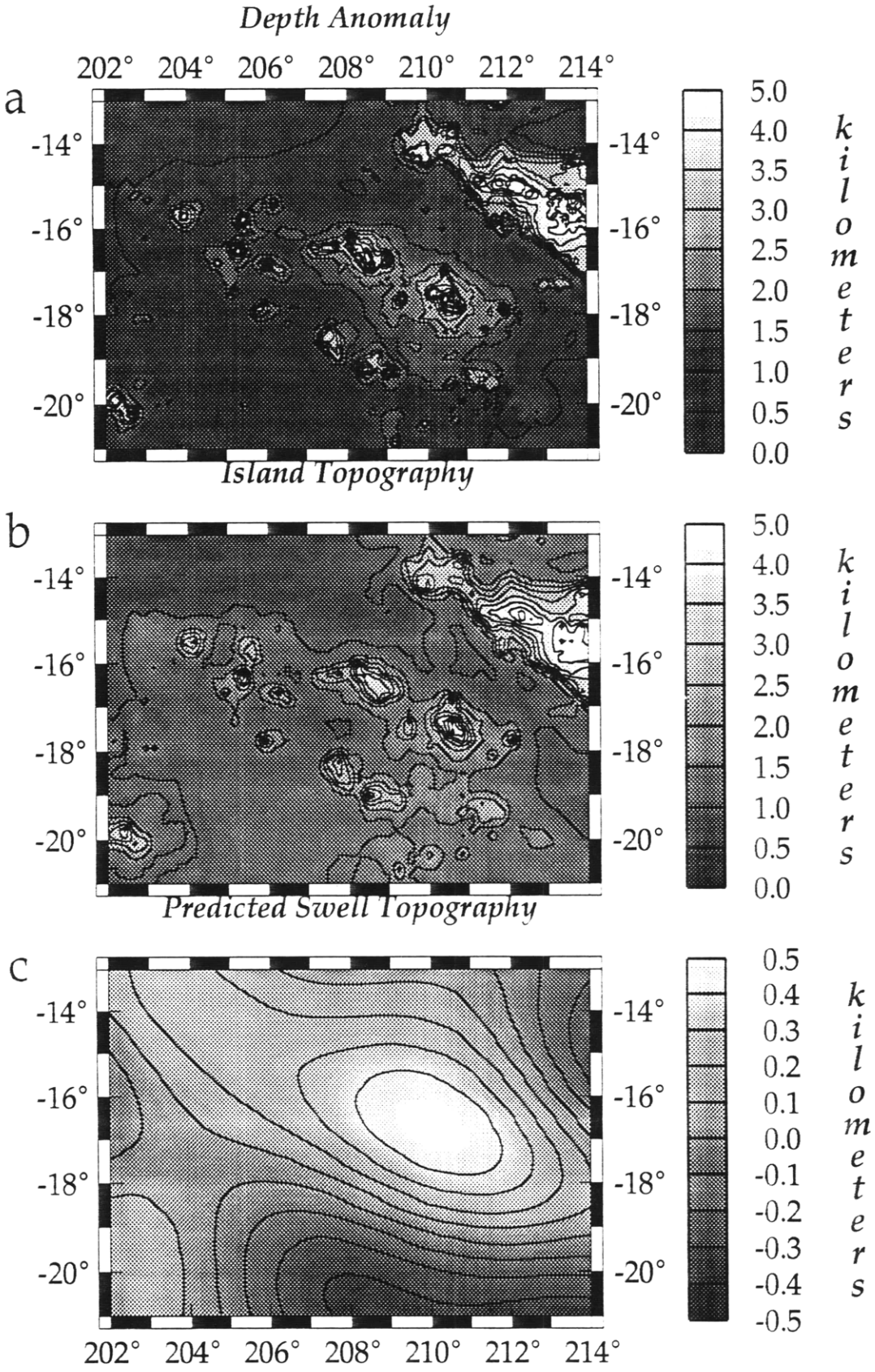
Depth Anomaly
a
202° 204° 206° 208° 210° 212° 214°
-14°
-16°
-18°
-20°
5.0
4.0
3.5
3.0
2.5
2.0
1.5
1.0
0.5
0.0
kilometers
Island Topography
b
Predicted Swell Topography
c
0.5
0.4
0.3
0.2
0.1
0.0
-0.1
-0.2
-0.3
-0.4
-0.5

Figure 3.3

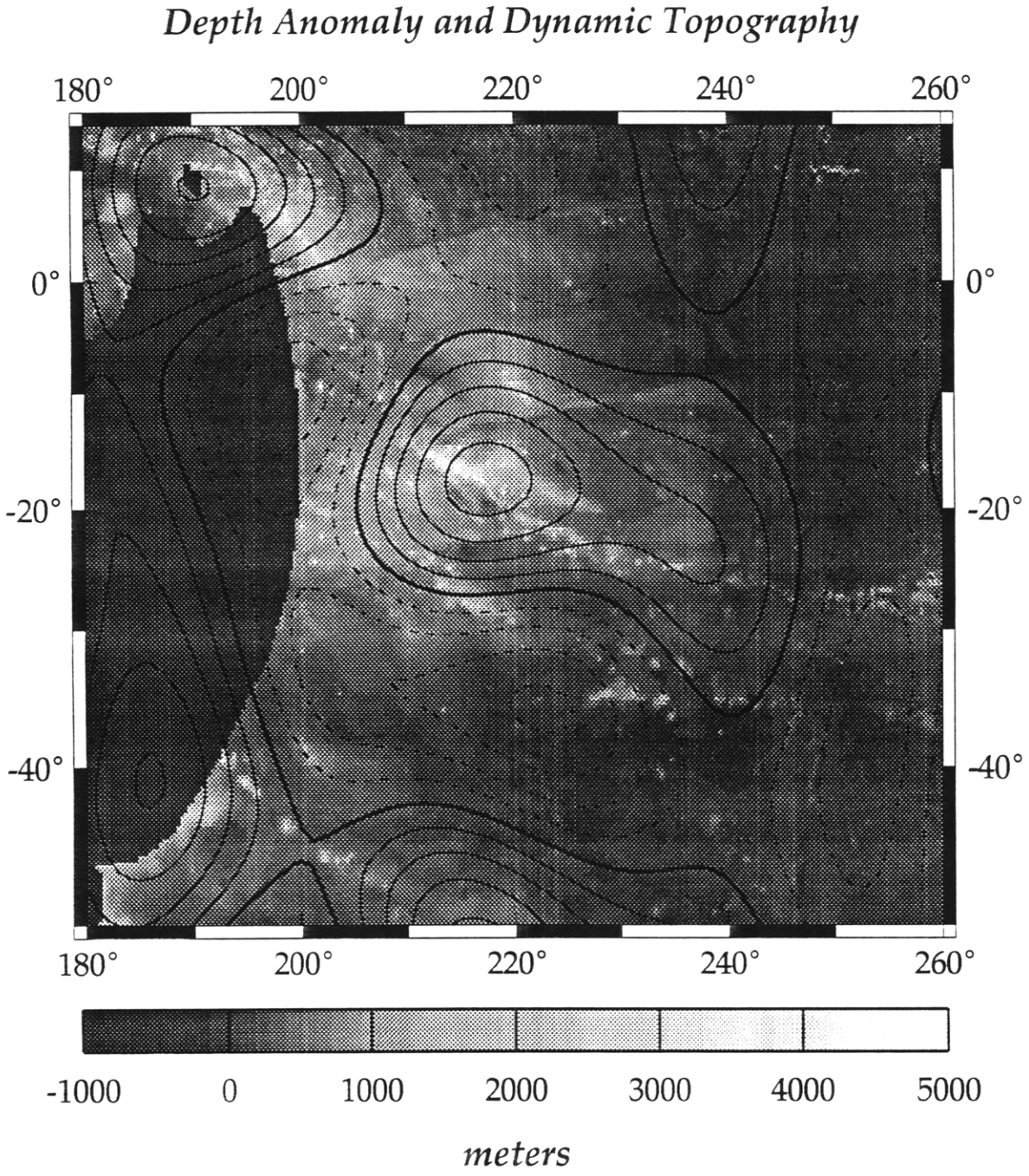
Depth Anomaly and Dynamic Topography
180°
200°
220°
240°
260°
0°
-20°
-40°
-1000
0
1000
2000
3000
4000
5000
meters

Figure 3.4

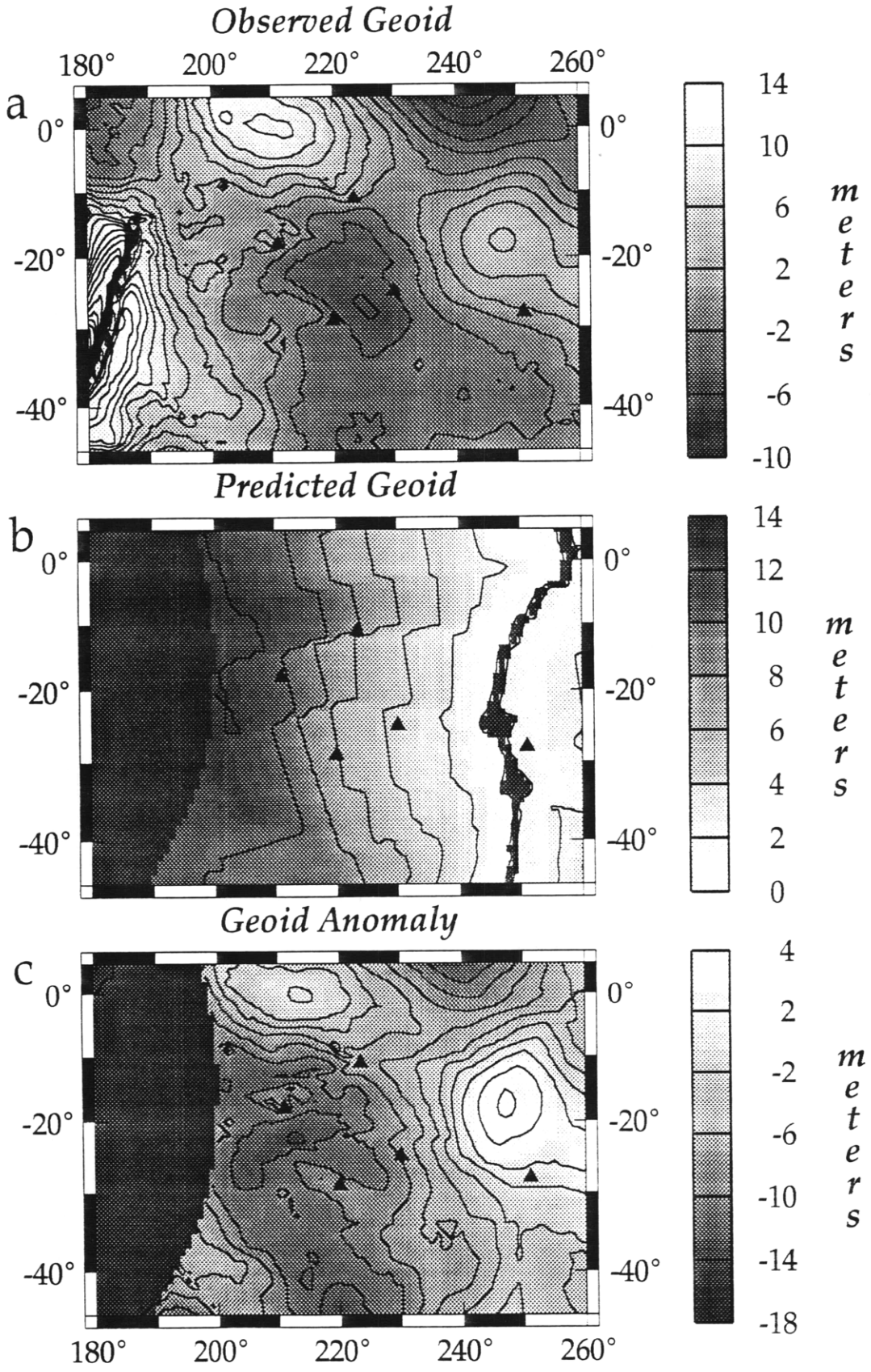
Observed Geoid
a
180°
200°
220°
240°
260°
0°
-20°
-40°
14
10
6
2
-2
-6
-10
meters
Predicted Geoid
b
14
12
10
8
6
4
2
0
meters
Geoid Anomaly
c
4
2
-2
-6
-10
-14
-18
meters

Figure 3.5

Chapter 4: Results

4.1 Tests of the Inversion Procedure

Before performing an inversion with the observed data, we test the inverse procedure by using forward modeled geoid and topography. The use of synthetic data allows testing of the stability of the inversion and provides indications of possible limitations of the inversion. We performed over 30 inversions using synthetic data with various input and reference viscosity profiles. The procedure for identifying the best-fit solution is described in section 2.2.

Since the problem is non-unique, there are a number of viscosity profiles which fit the data equally well, which are evidenced as multiple minima in χ^2. We explore a broad range of values of μ (10^{-12} to 10^{3}) to identify best-fit viscosity model. The inversion produces best results when the viscosity of the reference model is within an order of magnitude of the true viscosity profile. In these cases the viscosity within a particular layer is determined to within 15%. Two results are shown in Figure 4.1; the best-fit viscosity profiles are very close to the true solutions, and are different from the reference models. In some cases, minima in χ^2 exist for different values of μ, suggesting that the inversion identifies alternate solutions. When the reference model is close to the true solution, the differences in these alternate viscosity models are very small, implying that the inversion finds the same solution more than once. Thus, the inversion appears to be stable; once a solution is identified, further iterations determine viscosity profiles

increasingly different from the solution (corresponding to an increase in χ^2), but that the initial solution is identified again.

In test cases where one or more layers of the reference model differed from the true solution by an order of magnitude or greater, the inverse procedure is not as well behaved. In most of these cases, the inversion was not able to accurately determine the expected solution. One such example is shown in Figure 4.2. The inversion correctly increases the viscosity in the third layer relative to that of the second layer, but the magnitude of this contrast, as well as the contrast between the third layer and the lower mantle, are underestimated by an order of magnitude. The viscosity profile identified by the inversion fits the data and is a valid solution. In addition, the pattern and the amplitude of the predicted geoid and topography agree well with the synthetic data. By all objective criteria, we cannot determine that this solution is not the "true" viscosity profile.

These results pose a difficulty in determining the viscosity profile of the mantle based on observed data. If we use a reference model which is close to the true viscosity profile, the inversion will likely find the true solution. However, if we use a reference viscosity profile which is significantly different from the true viscosity, we may identify a completely different solution. Since the true viscosity is unknown, we have no way to determine if the reference viscosity is close to it and therefore cannot determine *a priori* if the inversion will be within its region of stability. In addition, in the above tests, the χ^2 goodness-of-fit was not significantly different for the true viscosity profiles and the alternate solutions found by the inversion. If multiple viscosity solutions have similar misfits to the data. and the patterns and amplitudes of the predicted fields match the data well, then we cannot determine objectively which solution is most likely to represent the true viscosity structure of the Earth's mantle.

4.2 Inversion of Data

We performed several inversions with the observed geoid and topography data using the viscosity profiles shown in Figure 1.1. Most of these profiles have been determined by modeling the global geoid field. Models SS1 - SS3, however, are retained from our forward modeling of the Superswell [*McNutt and Evans*, 1993], and are included to provide reference models with pronounced low viscosity zones to ensure that the inverse procedure explores this region of solution space. The results of three inversions are shown in Figure 4.3; most of the data inversions identify two χ^2 minima, which correspond to different viscosity solutions. If the minima in χ^2 are comparable, the viscosity model corresponding to the minima with the larger value of μ is the best-fit model, because it is closer to the reference model. Several of the alternate solutions found in these inversions are virtually identical to best-fit solutions for other reference models. The fact that these solutions are found in separate inversions, using reference models in which viscosity in a layer differs greater than an order of magnitude shows that this procedure identifies consistent solutions, and implies that this inversion procedure is stable.

Seventeen viscosity profiles determined by these inversions represent five distinct classes of viscosity models, shown in Figure 4.3. These solutions retain the general character of the reference models used for the inversion, but the viscosity in at least one layer differs from that of the reference model by at least a factor of 3. This implies that the solution is not constrained to be too close to the reference model, and a solution which fits the data well can be identified. The rms misfit to the data for the reference models used is listed in Table 4.1. Some of these models (e.g. K2, SS1) provide a poor fit to the data, whereas others reasonably fit the data (e.g. MODSH, MDLSH, SH425). The five viscosity solutions which we determine, models A through E, and their corresponding reference models are listed in Table 4.2. In all cases, our solutions provide misfits to the data which is less than or equal to that of the reference models.

The patterns and magnitudes of the predicted geoid fields differ greatly for these viscosity solutions. The peak-to-trough amplitude of the predicted geoid for model A is extremely small, 0.15 m, (Figure 4.5) and it is negatively correlated with the pattern in the observed geoid. The locations of highs and lows in the geoid predicted by models B and E are correct, but their peak-to-trough amplitudes considerably underestimate that observed. Models C and D predict geoid fields which agree well with the pattern of the data, and under-predict the amplitude of the geoid and dynamic topography the least (Figure 4.5). Of the five viscosity models identified by the inversion, we conclude that models C and D are the most consistent with both sets of data.

Table 4.1 Data Misfits for Reference Models

Reference Model	Misfit to data, χ^2
SS1	80.88
SS2	77.52
SS3	61.03
HCW4	63.64
HCW4b	78.89
K1	46.68
K2	383.44
CT	78.73
MODSH	48.13
MDLSH	46.53
SH425	46.88

Table 4.2 Reference Models and Data Misfits for Viscosity Solutions

Solution	Misfit to data, χ^2	Reference Models
A	49.35	SS1, CT
B	46.72	SS1, SS2, HCW4b, CT
C	46.60	SS3, HCW4
D	46.60	MODSH, MDLSH, SH425
E	46.84	K1, K2

Figure Captions

Figure 4.1. Results from two test inversions using synthetic geoid and topography data. Left: plot of χ^2 vs. μ on a logarithmic scale. The asterisk denotes the misfit to the data of the best-fit viscosity solution which is shown on the right. Right: The reference viscosity solution used for the inversion (dotted line), the "true" viscosity profile used to generate the synthetic data (solid line), and the best-fit viscosity model corresponding to the asterisk in the left plot (dash-dot line). a) Test results using model SS1 as a reference model and data generated using model SS3. The best-fit solution exactly coincides with the true solution in all layers except layer 3, where it is different by about 10%. b) results using model SH425 as a reference model and model MODSH to generate the data. Again, the best-fit solution nearly coincides with the true solution in every layer. In both of these tests, the inversion succeeded in finding the true viscosity model.

Figure 4.2. Results of a test inversion using synthetic data, as in Figure 4.1. The reference model used is HCW4b and the model used to generate the synthetic data is HCW4. Note that the best-fit solution found by the inversion does not approximate the true solution. The difference in viscosity between the reference and true solutions in the third layer is greater than an order of magnitude. Tests such as this show that if the difference between the reference and true solutions is greater than an order of magnitude, then the inverse procedure has difficulty locating the true solution.

Figure 4.3. Results of an inversion using the observed geoid and topography data. The solid line represents the reference viscosity model used in the inversion, the dash-dot line is the solution corresponding to the asterisk in the data misfit plot, and the dotted line corresponds to the circle in the data misfit plot. The horizontal dashed line in the left plot indicates the misfit to the data of the reference model. a) Results of data inversion using model SS3 as the reference model. Two different solutions with comparable χ^2 are found, both of which have a misfit to the data much less than the reference model. b) Results of a data inversion using model SS2 as a reference model. One solution is found, and χ^2 is much lass than that of the reference model.

Figure 4.4. Seventeen viscosity solutions were identified by inverting the data using eleven different reference models. Several of these solutions were nearly coincident, and they are grouped into five distinct classes of viscosity models shown here. Three models are shown on the left: model A (solid line), model B (dashed line), and model C (dash-dot line). On the right, model D is represented by a solid line, and model E by a dashed line. Models D and E have been offset horizontally for clarity; these viscosity profiles represent relative changes in viscosity, not the absolute viscosity. Although all of these models predict similar values of χ^2, only models C and D satisfy both geoid and topography data.

Figure 4.5. Predicted and observed topography (top) and geoid (bottom) for the five viscosity solutions. Grayscale indicates observed data and contours represent predicted data. Solid contours represent positive values, dashed contours represent negative values, and the thick solid line indicates the zero contour. Contours are 500 m for topography and 1 m for geoid unless otherwise noted. Black triangles mark the locations where the predicted fields and the misfit to the data are calculated. a) Predicted data for model A. The general pattern and sign of the topography are matched, but the geoid is of opposite sign and very small magnitude (0.05 m contours). b) Predicted data for model B. The patterns of the topography and geoid are relatively well matched, but the magnitude of the geoid is rather small (4 m peak-to-peak). c,d) Predicted data for models C and D. The patterns of both the geoid and topography are well matched, and their amplitudes are reasonable. These topography solutions represent our preferred solutions. e) Predicted data for model E. The patterns in the topography and geoid are roughly coincident with the observed, but the magnitude of the predicted geoid is rather small.

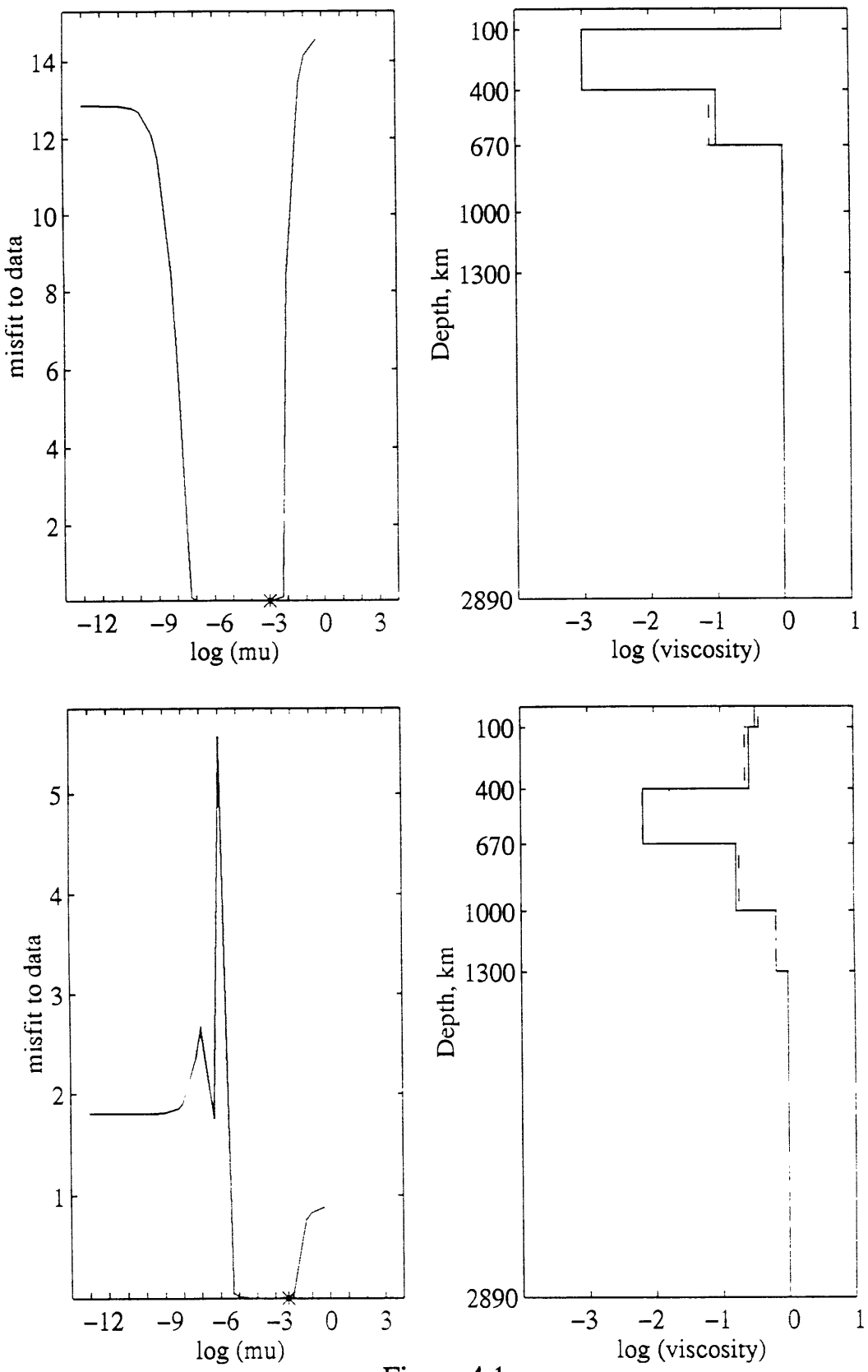
misfit to data
log (mu)
Depth, km
log (viscosity)
misfit to data
log (mu)
Depth, km
log (viscosity)

Figure 4.1

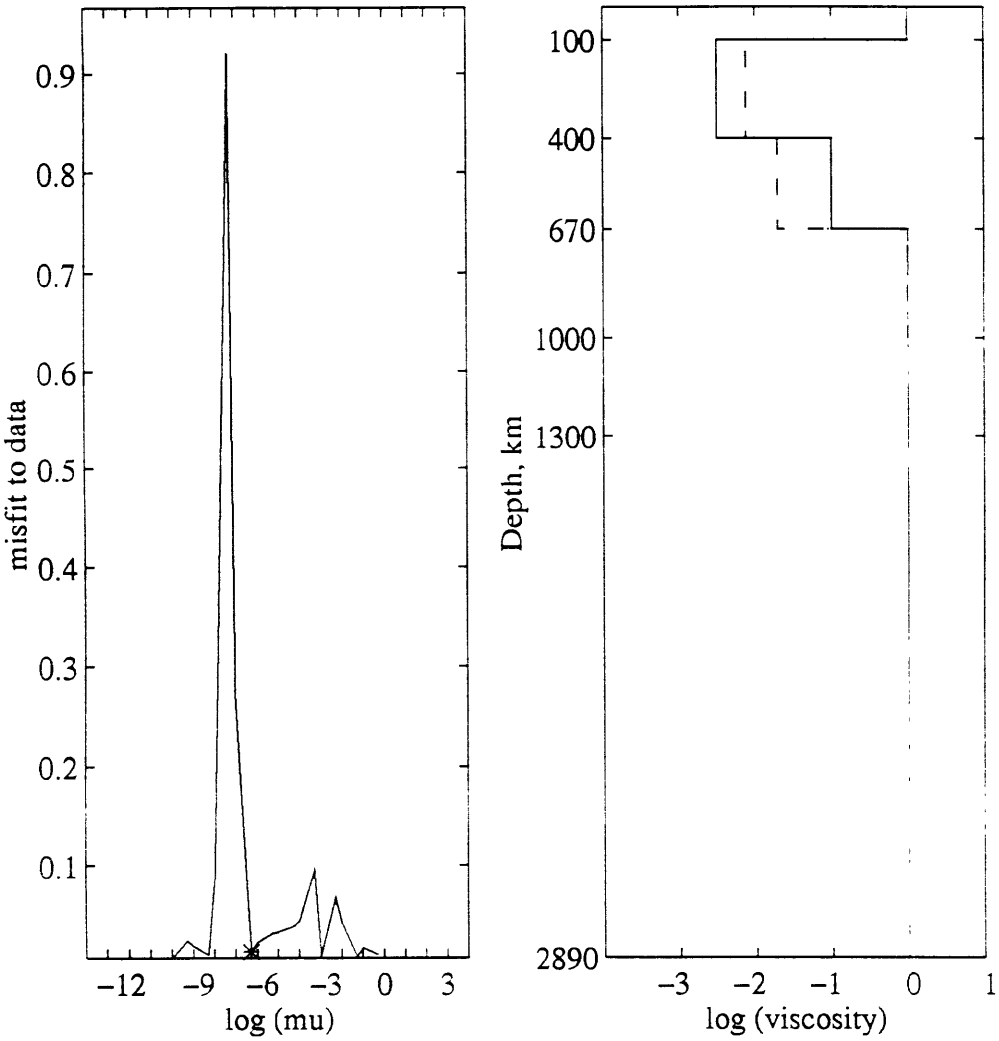
misfit to data
0.9
0.8
0.7
0.6
0.5
0.4
0.3
0.2
0.1
−12
−9
−6
−3
0
3
log (mu)
Depth, km
100
400
670
1000
1300
2890
−3
−2
−1
0
1
log (viscosity)

Figure 4.2

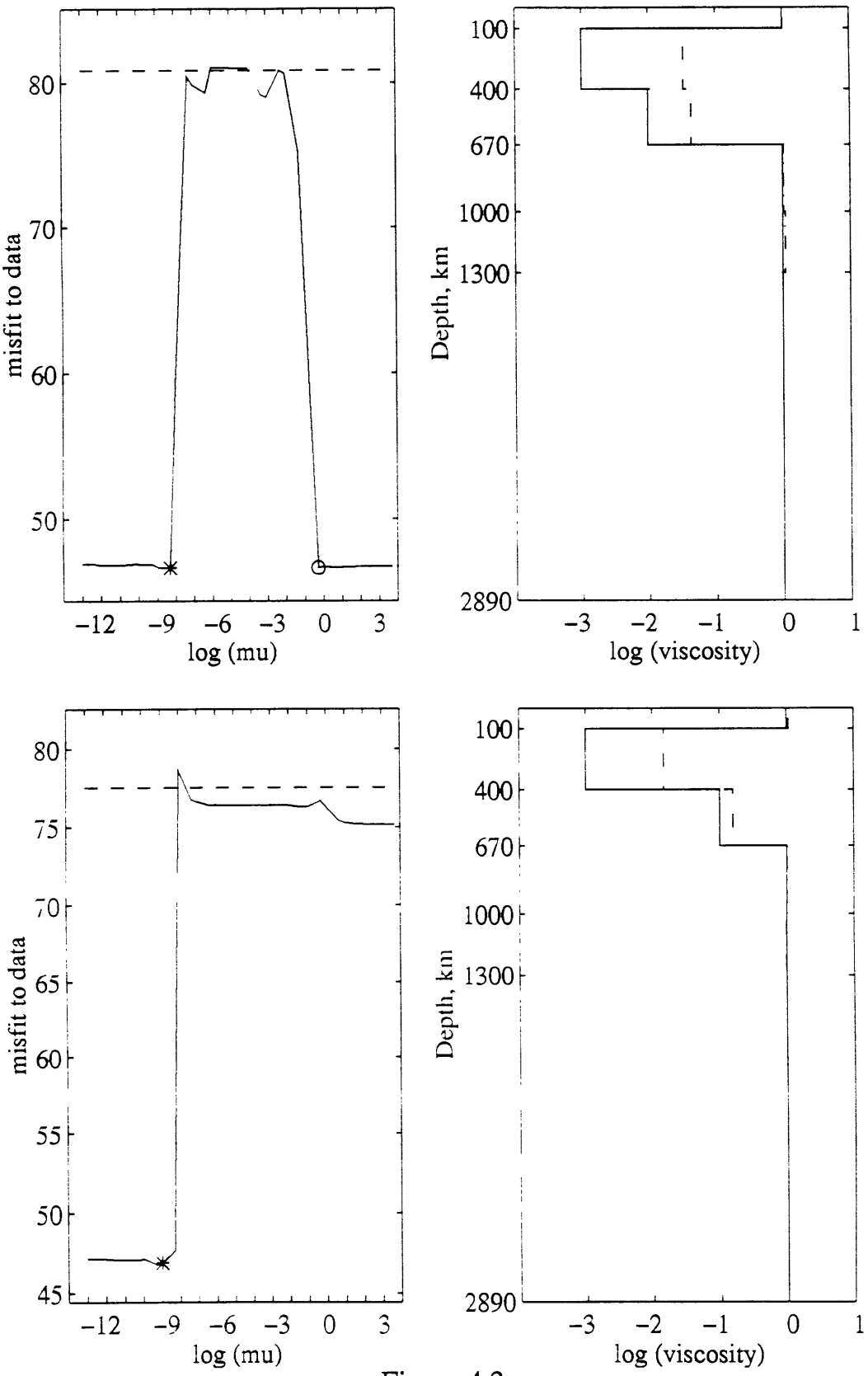
misfit to data
80
70
60
50
−12 −9 −6 −3 0 3
log (mu)
Depth, km
100
400
670
1000
1300
2890
−3 −2 −1 0 1
log (viscosity)
misfit to data
80
75
70
65
60
55
50
45
−12 −9 −6 −3 0 3
log (mu)
Depth, km
100
400
670
1000
1300
2890
−3 −2 −1 0 1
log (viscosity)

Figure 4.3

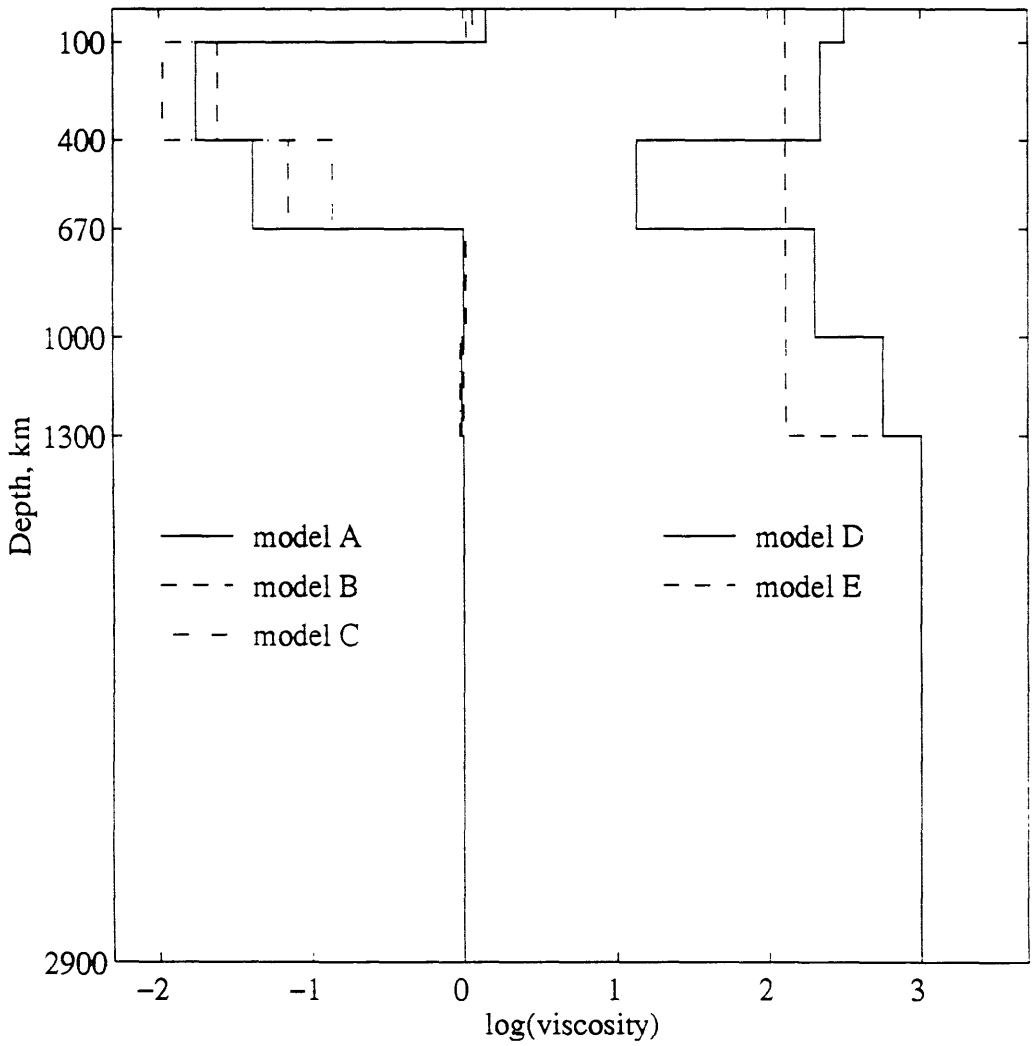
100
400
670
1000
1300
2900
Depth, km
model A
model B
model C
model D
model E
−2
−1
0
1
2
3
log(viscosity)

Figure 4.4

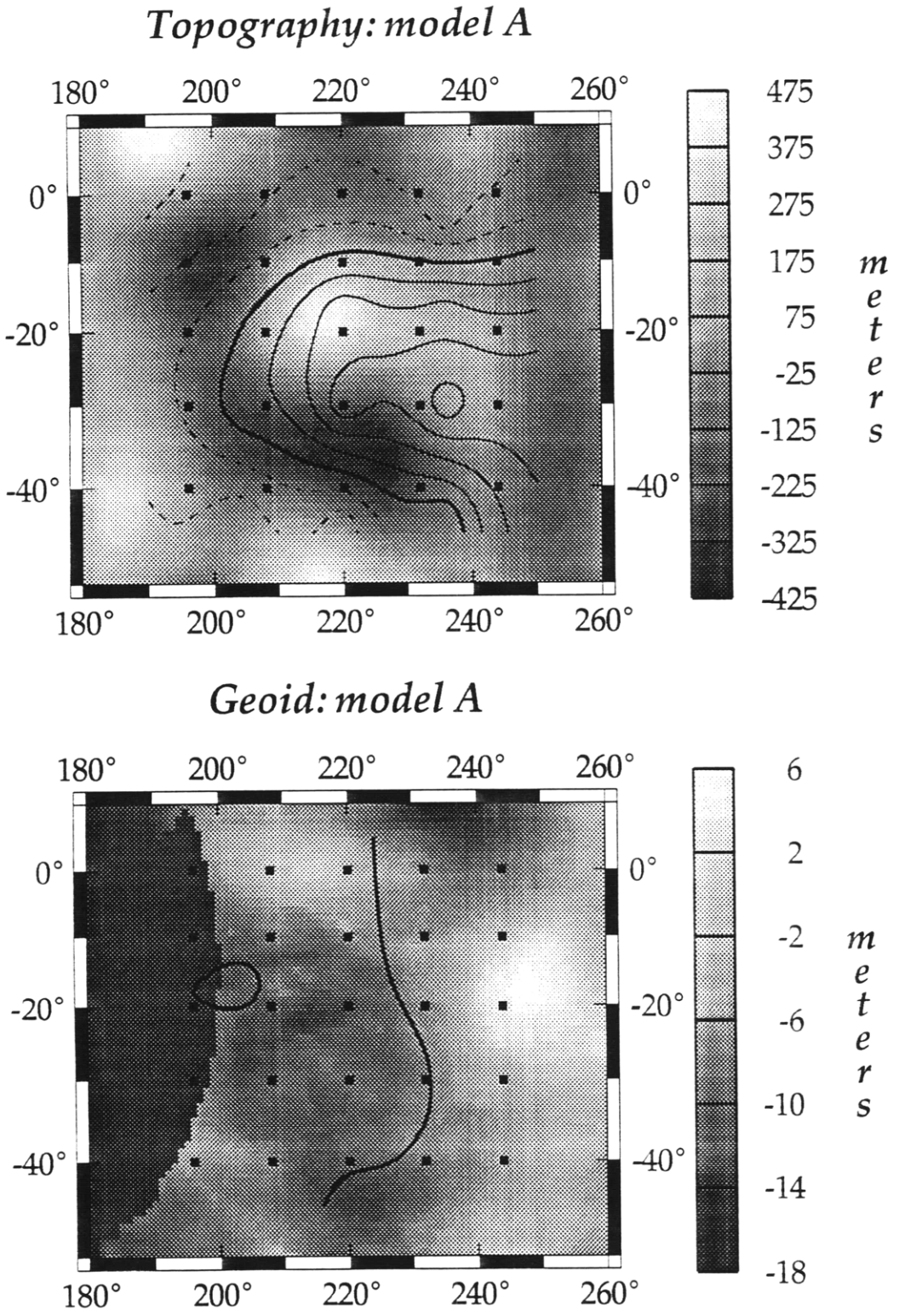
Topography: model A
180°
200°
220°
240°
260°
0°
-20°
-40°
475
375
275
175
75
-25
-125
-225
-325
-425
meters
Geoid: model A
6
2
-2
-6
-10
-14
-18
meters

Figure 4.5a

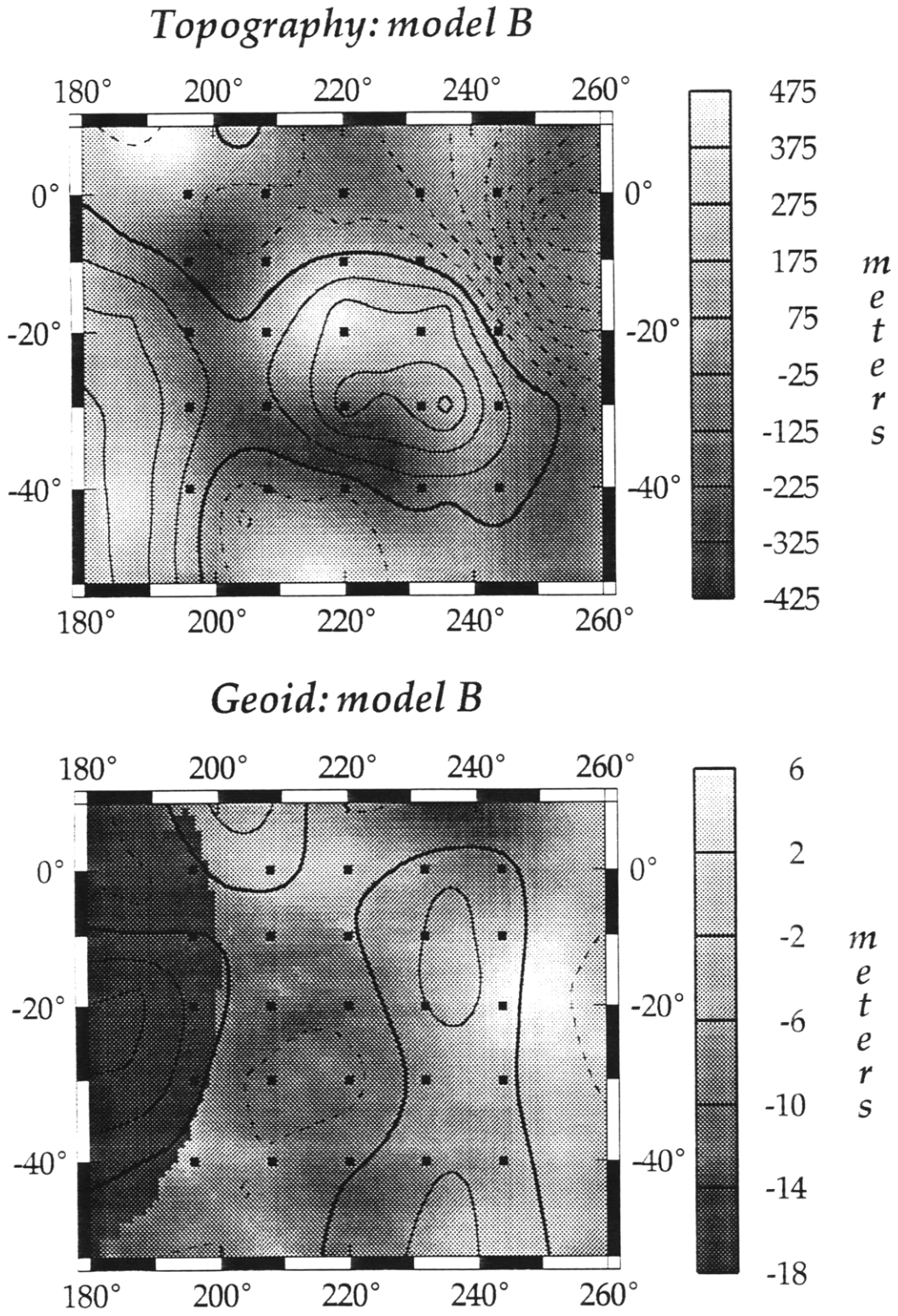
Topography: model B
180°
200°
220°
240°
260°
0°
-20°
-40°
475
375
275
175
75
-25
-125
-225
-325
-425
meters
Geoid: model B
6
2
-2
-6
-10
-14
-18

Figure 4.5b

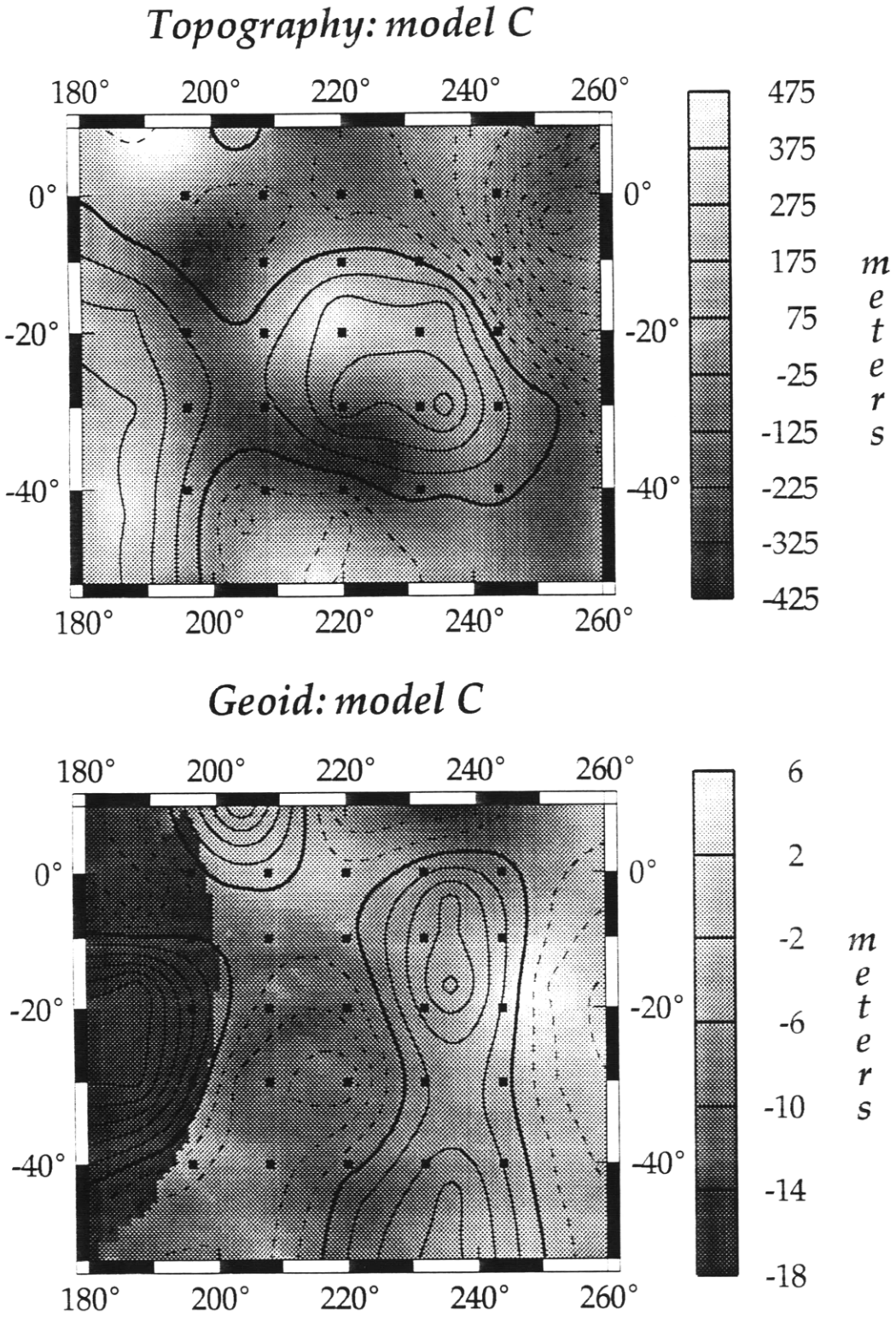
Topography: model C
180°
200°
220°
240°
260°
0°
-20°
-40°
475
375
275
175
75
-25
-125
-225
-325
-425
meters
Geoid: model C
6
2
-2
-6
-10
-14
-18

Figure 4.5c

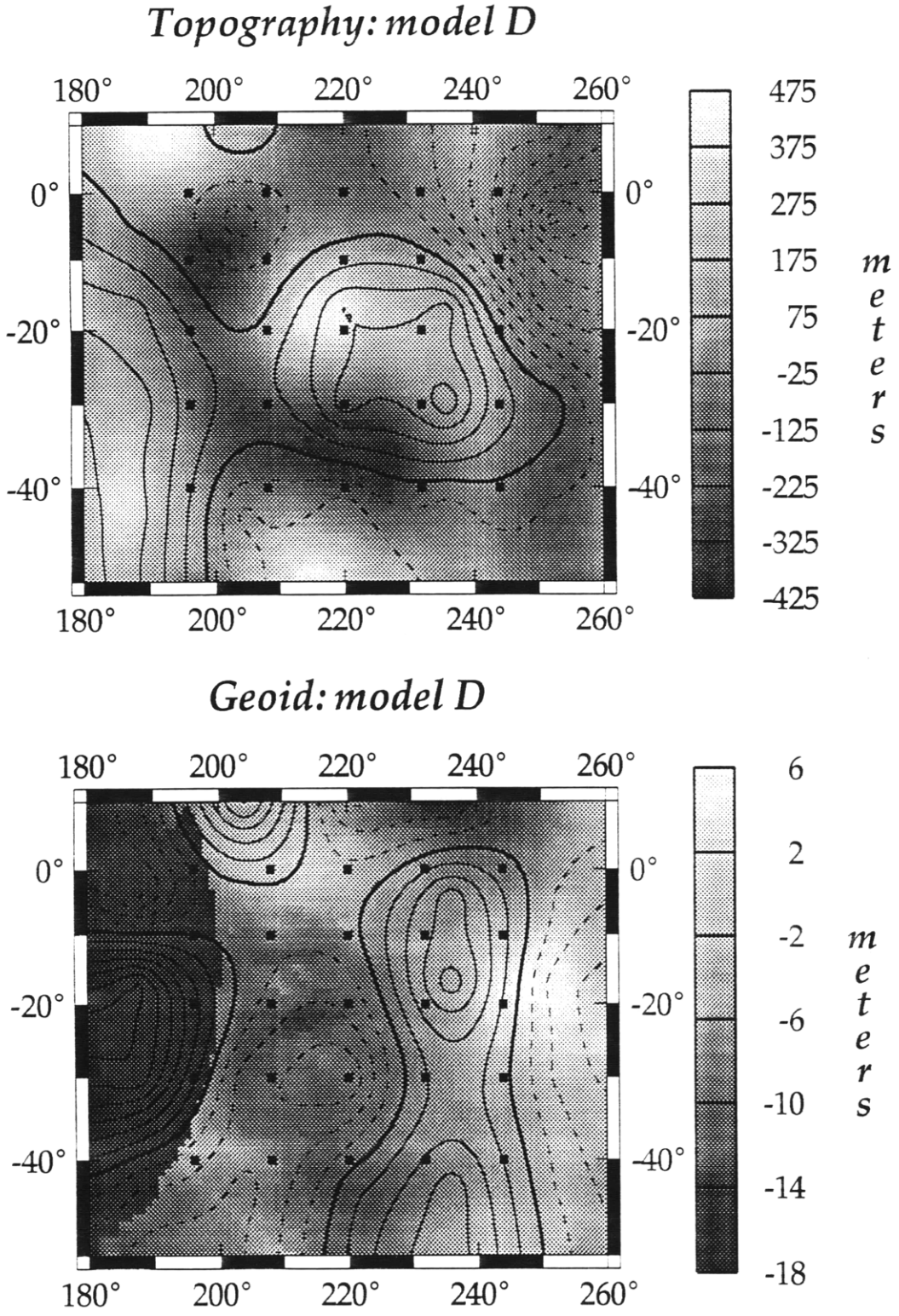
Topography: model D
180°
200°
220°
240°
260°
0°
-20°
-40°
475
375
275
175
75
-25
-125
-225
-325
-425
meters
Geoid: model D
6
2
-2
-6
-10
-14
-18

Figure 4.5d

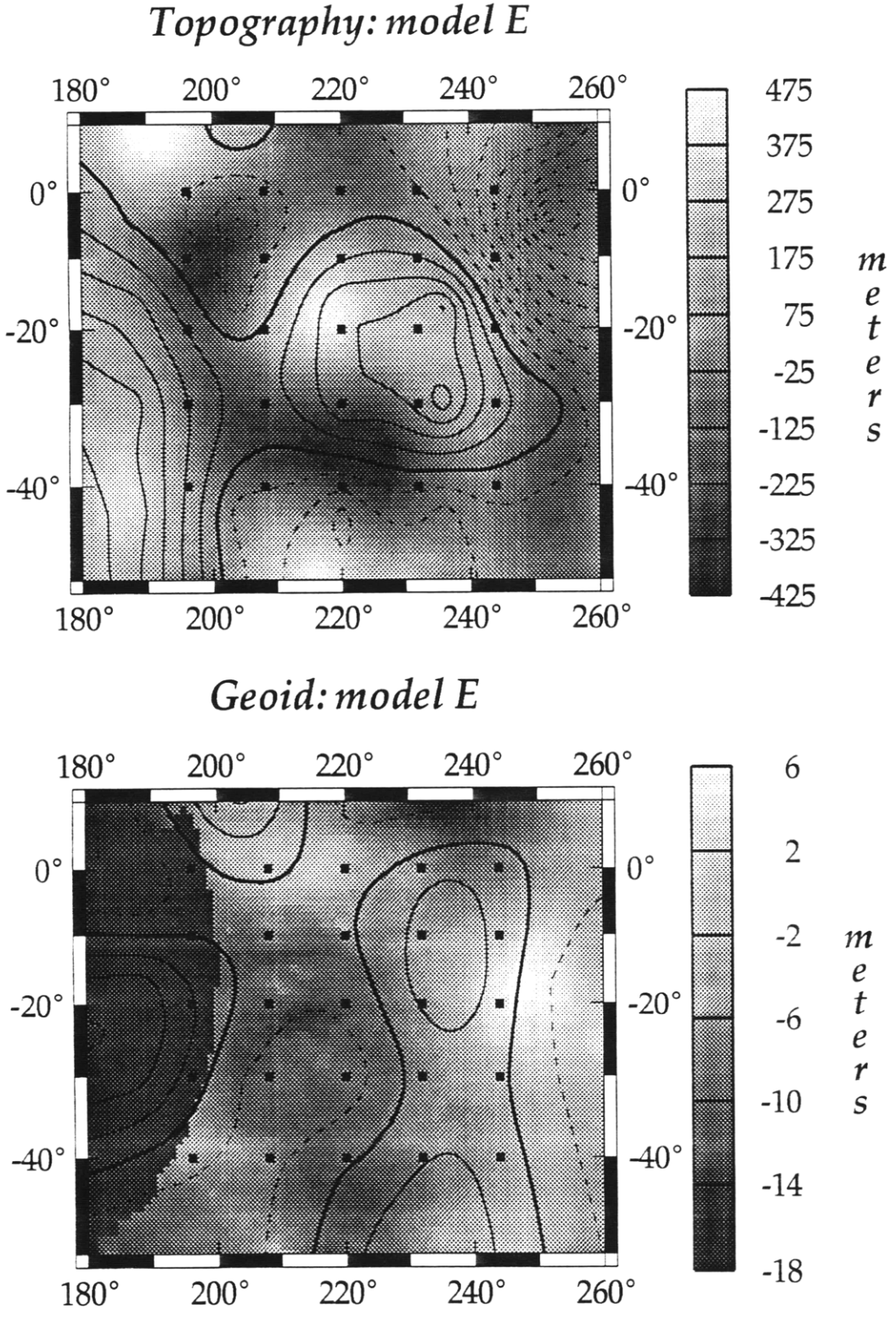
Topography: model E
180°
200°
220°
240°
260°
0°
-20°
-40°
475
375
275
175
75
-25
-125
-225
-325
-425
meters
Geoid: model E
6
2
-2
-6
-10
-14
-18

Figure 4.5e

Chapter 5: Discussion

In calculating the geoid and topography kernels via equations (2.4-2.5), we have assumed that the mantle behaves as an incompressible, Newtonian fluid in which viscosity is radially symmetric. These assumptions are not strictly true, and the validity of these approximations should be addressed.

This study, and most previous studies [*Hager and Clayton*, 1989; *Hager and Richards*, 1989; *King and Masters*, 1992; *Kogan and McNutt*, 1992] have assumed that the mantle is incompressible for mathematical simplicity. However, it is known that gravity increases from 9.8 m s^{-2} to 10.7 m s^{-2} from the surface to the core-mantle boundary, and that density increases by a factor of two throughout the mantle [*Dziewonski and Anderson*, 1981]. Compressible geoid kernels are up to 10% larger in peak-to-peak magnitude than incompressible geoid kernels, but this difference decreases with increasing harmonic degree [*Forte and Peltier*, 1991]. At degrees 8 through 12, this difference is roughly 5% [S. Panasyuk, personal communication], and therefore should not significantly effect our results.

In formulating this problem, we have explicitly assumed that a density contrast of a given degree and order can produces velocities and stresses only at the same degree and order. If this assumption holds, the different harmonic terms represented in (2.4-2.5) can be separated and solved for independently. The separation of harmonic terms holds only if viscosity is truly a function of radius only. If lateral variations in viscosity result from

a temperature- or stress-dependent rheology, then a pure harmonic density contrast induces flow for several spectral terms [*Richards and Hager*, 1989; *Cadek et al.*, 1993]. Then, the terms in (2.4-2.5) remain coupled and must be solved simultaneously.

Viscosity is known to vary laterally within the mantle; in searching for variations to a global average viscosity structure, we explicitly assume that lateral variations in viscosity occur. The scale at which these variations are significant is unknown. We assume that within the region of examination, lateral variations of viscosity are small in magnitude. The upper mantle beneath the Superswell is not likely to possess large variations in viscosity. This are is underlain by oceanic upper mantle which is devoid of subduction zones, thus horizontal changes in chemistry should be minimal. If lateral variations in viscosity within our region are non-negligible, mode coupling between density, geoid and dynamic topography will occur.

Laboratory studies of polycrystalline silicates suggest a non-linear stress-strain relation at high temperatures and pressures. Therefore a non-linear stress-dependent rheology may be appropriate for the mantle. *Cadek et al.* [1993] have performed mantle convection calculations predicting geoid fields for both linear and non-linear ($n = 3$) rheologies. They find that the strongest coupling of the geoid field occurs at three times the harmonic degree of the density perturbation. For example, a degree 2 density structure couples strongest with the degree 6 geoid, inducing a signal which is 26% of the amplitude of the degree 2 geoid [*Cadek et al.*, 1993]. Since the spectral power of the geoid falls off rather quickly [*Lerch et al.*, 1994], the relative amount of degree 8-12 geoid structure which is induced by degree 3 and 4 density structure could be substantial. However, numerical experiments indicate that the overall effect of a non-linear rheology is to increase the amplitude of the geoid, without strongly effecting the spatial pattern [*Cadek et al.*, 1993]. Given the present uncertainties in mantle density structure, seismic to density scaling relations and possible viscosity structures, the errors involved in assuming a Newtonian rheology are small in comparison [*Cadek et al.*, 1993].

Another simplifying assumption in our calculations is that density variations within the mantle are linearly related to variations in shear wave velocity. However, this scaling relationship is not well determined. Since this value enters as a multiplicative factor in (2.15), there is a tradeoff between the value of this parameter and the magnitude of viscosity variations. $\partial \ln v_s / \partial \ln \rho$ varies laterally within the upper mantle, reflecting chemical differences between subducted slabs and oceanic and continental upper mantle. Temperature and pressure changes with depth also cause this parameter to vary with depth.

Room-temperature laboratory measurements of silicate minerals can provide estimates of this value, but it cannot be accurately determined at appropriate temperatures and pressures. Previous calculations of viscosity have estimated this parameter using laboratory measurements [*King and Masters*, 1992], correcting these measurements with temperature and pressure derivatives of mineral properties [*Forte and Peltier*, 1991], and performing a linear least-squares inversion of geoid data [*Hager and Clayton*, 1989; *Forte et al.*, 1993]. We have chosen to adopt a constant value of this parameter in our calculations. Since we limit our analysis to a region which encompasses oceanic upper mantle only, lateral variations of $\partial \ln v_s / \partial \ln \rho$ due to chemistry should be minimal. In addition, we limit our analysis to the upper portion of the mantle where depth-related pressure and temperature induced variations should also be small.

The data sets which are used in the inversion have a large effect on the resulting solution. The largest source of uncertainty in these calculations is the estimation of mantle density anomalies. Although the seismic velocity model, SH12/WM13, performed well in resolution tests, it is represented as a spherical harmonic field and therefore is limited in small-scale horizontal resolution. The dependence of our solutions on the velocity model could be tested in a future experiment by using different seismic velocity models. It is likely that block models, as opposed to spherical harmonic models will provide more detailed structure for a regional inversion such as this.

The fact that the inversion identifies more than one viscosity model which adequately fits the data is not surprising. The mathematics of the problem is inherently non-unique; the observed quantities are integrals based on the function that we wish to determine (2.15). Of these five solutions determined by the inversion, only two, models C and D, sufficiently satisfy the data. However, it is unclear whether either of these models represent the actual viscosity structure of the Earth's mantle.

It is puzzling that viscosity models A through E, whose model predictions have the same misfit to the data, should predict geoid fields which are very different from each other. This result appears to be an artifact of calculating the misfit to the data in the spatial domain. The misfit to the data, χ^2, is a measure of the difference in the magnitude of the predicted and observed fields at a finite number of points; it does not measure how well the patterns of the two fields correlate. It is possible for a predicted geoid or topography field which appears to be "close" to the observed data to have a higher χ^2 than a field which appears to be very different from the observed field. For example, consider a predicted geoid field which matches the pattern and magnitude of the observed field, but is shifted in phase. Since the misfit of the data is determined by measuring the difference of these fields at a finite number of points, the predicted field may have a high value of χ^2. A different viscosity model may predict a geoid field which does not match the observed field in pattern, phase, or amplitude, yet yields a smaller misfit to the data. An example of such a situation in two dimensions is shown in Figure 5.1. Thus, χ^2 is not an accurate measure of the goodness-of-fit between the predicted and observed data.

Calculating χ^2 in the spectral domain would assure a better fit between the patterns of the predicted and observed fields. However, it is unclear how to calculate the correlation between two spherical harmonic fields in a limited spatial region. The pattern of peaks and troughs in both the predicted geoid and topography do not exactly coincide with that of the observed data for any of the viscosity models examined here. Therefore

is it likely that viscosity models in which the overall pattern of the predicted fields more closely approximates that observed predict a high χ^2, and are thus overlooked in the inversion.

The lack of radial resolution in the prediction of data (2.12-2.13) also contributes to the difficulty of the inversion in identifying satisfactory viscosity solutions. The radial resolution of the kernels cannot be increased simply by increasing the number of viscosity layers in the model, because increasing the number of degrees of freedom in the inversion makes the Jacobian matrix ill-conditioned and causes the inversion to become more unstable. This problem can be overcome by increasing the number of radial shells for the prediction of data, but constraining the viscosity to be constant within several adjacent shells. This modification would allow more accurate prediction of geoid and topography data, while retaining the radial resolution of the seismic data, and limiting the number of effective viscosity layers.

Figure Captions

Figure 5.1. A simple example illustrating why χ^2 does not provide a good measure of the goodness-of-fit between predicted and observed data. a) In this example, the data is represented by a simple sine curve shown by the solid line. Model 1 is shown by the dotted line; it has the same amplitude and shape as the data, but is shifted in phase by 13 units. The rms misfit to the data, χ^2, for model 1 is 0.32 and is represented by the shaded area in the figure. b) The data is again shown by the solid line and model 2 illustrated by the dotted line. Model 2 differs from the observed data in amplitude, shape, and phase. Yet its misfit to the data, χ^2, is 0.30, which is less than that of model 1. Model 1 provides a better visual fit to the data, yet model 2 provides the better mathematical fit to the data.

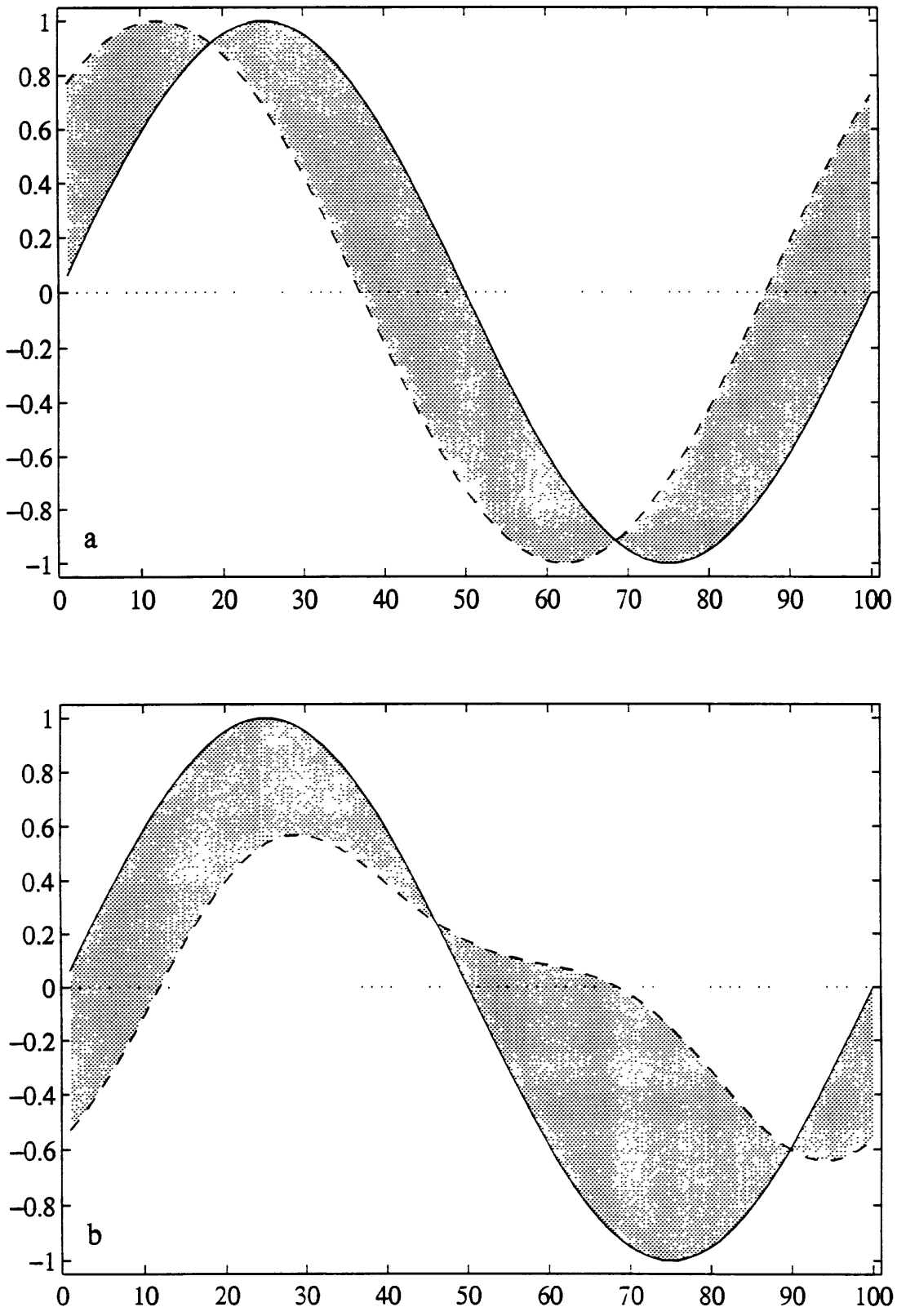

Figure 5.1

Chapter 6: Conclusions

This inverse procedure we have developed appears to be promising to determine variations to reference viscosity models to fit regional geoid an topography data. In synthetic tests, this procedure is well-behaved if the true viscosity profile is within an order of magnitude of the reference model. In other words, this technique can accurately determine a viscosity solution which is a small perturbation to the reference model. If the reference model is far from the true solution, this procedure will either fail to find a solution or identify an alternate solution. However, two limitations of this technique remain. In its current formulation, the radial parameterization used to predict the geoid and topography is very poor, and much radial resolution is lost in the uppermost mantle where the geoid and topography kernels are highly variable. This lack of resolution decreases the difference in the predicted geoid and topography fields for slightly differing viscosity profiles. This diminishes the ability of the inversion to discriminate between possible viscosity solutions and most likely precludes the determination of valid viscosity solutions. In addition, this problem contributes to the inability of the inversion to determine the correct viscosity solution if it is much different from the reference model. This limitation is straightforward to remedy, and will be corrected in a continuation of this study.

A second limitation of this technique is the manner in which the goodness-of-fit of the model predictions to the data is calculated. As illustrated in Figure 5.1, the rms

misfit, χ^2, is not an accurate measure of the goodness-of-fit between the predicted and observed data. This quantity measures the difference in the magnitudes of the fields, but does not characterize the differences in the spatial patterns. A more accurate method to measure the differences between the patterns of these fields would be to calculate the goodness-of-fit in the spectral domain. However, the geoid and topography are predicted in terms of spherical harmonic coefficients, and it is unclear how to calculate the correlation between harmonic coefficients in a limited spatial domain. The result of this limitation is that some of the viscosity solutions identified do not satisfactorily fit the data, despite their small rms misfit. In addition, viscosity profiles whose model predictions fit the data well are likely overlooked due to their deceptively large rms misfits.

The current formulation of the procedure, identifies two viscosity profiles which are consistent with the observed geoid and topography data. Due to the non-uniqueness of this problem, it is not surprising that more than one solution was identified. However, how do we determine if either solution represents the true viscosity of the Earth's mantle? Both solutions are consistent with the observed geoid and topography data, seismic velocity models provide other discriminatory information. The shear wave velocity anomalies are strongest above 400 km depth, and the pattern of the velocities at depths between 100 and 400 km correlates most strongly with the pattern in the observed geoid and topography. Since the magnitude of the seismic velocity variations are greater at depths of 100-400 km than at depths between 400 and 670 km, it follows that the largest variation in temperature-induced viscosity variations would occur at the same depth. For this reason, we favor model C as a preferred solution. We envision hot material at the base of the lithosphere representing the top of a mantle plume which has impinged on the lithosphere. The increased temperatures in this region (approximately 300° C) result in lower viscosities. Since stresses are attenuated in this low viscosity layer, the buoyancy forces associated with the hot, low density material create a small amount of surface

uplift. The net geoid anomaly is then negative, since the negative geoid signal from the buoyant, low density material is greater in magnitude than the positive geoid signal from the surface uplift. The presence of hot material beneath the lithosphere is also consistent with the large number of volcanic islands in this region of the seafloor; this material conductively warms the base of the lithosphere, increasing the probability of volcanic activity.

References

Cadek, O., Y. Ricard, Z. Martinec, and C. Matyska, Comparison between Newtonian and non-Newtonian flow driven by internal loads, *Geophys. J. Int.*, 112, 103-114, 1993.

Cazenave, A., and C. Thoraval, Mantle dynamics constrained by degree 6 surface topography, seismic tomography and geoid: Inference on the origin of the South Pacific Superswell, *Earth Planet. Sci. Lett.*, **122**, 207-219, 1994.

Constable, S. C., R. L. Parker, and C. Constable G., Occam's Inversion: A practical algorithm for generating smooth models from electromagnetic sounding data, *Geophysics*, **52**, 289-300, 1987.

DeMets, C., R. G. Gordon, D. F. Argus, and S. Stein, Current plate motions, *Geophys. J. Int.*, **101**, 425-478, 1990.

Dziewonski, A. M., and D. L. Anderson, Preliminary reference Earth model, *Phys. Earth Planet. Int.*, **25**, 297-356, 1981.

Filmer, P. E., M. K. McNutt, and C. J. Wolfe, Elastic thickness of the lithosphere in the Marquesas and Society Islands, *J. Geophys. Res.*, **98**, 19,565-19,578, 1993.

Forte, A. M., A. M. Dziewonski, and R. L. Woodward, Aspherical structure of the mantle, tectonic plate motions, nonhydrostatic geoid, and topography of the core-mantle boundary, in *Dynamics of Earth's Deep Interior and Earth Rotation*, edited by J.-L. Le Mouel Smylies, D. E., and T. Herring, *Geophysical Monograph*, 72, pp. 135-166, IUGG and AGU, Washington, D. C., 1993.

Forte, A. M., and W. R. Peltier, Viscous flow models of global geophysical observables: 1. Forward problems, *J. Geophys. Res.*, **96**, 20,131-20,159, 1991.

Hager, B. H., and R. W. Clayton, Constraints on the structure of mantle convection using seismic observations, flow models, and the geoid, in *Mantle Convection*, edited by W. R. Peltier, pp. 657-763, Gordon and Breach, New York, 1989.

Hager, B., H., and R. J. O'Connell, A simple global model of plate dynamics and mantle convection, *J. Geophys. Res.*, **86**, 4843-4867, 1981.

Hager, B. H., and M. A. Richards, Long-wavelength variations in Earth's geoid: physical models and dynamical implications, *Phil. Trans. R. Soc. Lond.*, **328**, 309-327, 1989.

Judge, A. V., Some implications of the earth's potential field for structure in the mantle, *General Exam Paper*, MIT, 1986.

King, S. D., Radial models of mantle viscosity: Results from a genetic algorithm, *Geophys. J. Int.*, *submitted*, 1993.

King, S. D., and G. Masters, An inversion for radial viscosity structure using seismic tomography, *Geophys. Res. Lett.*, **19**, 1551-1554, 1992.

Lerch, F. J., et al., A geopotential model from satellite tracking, altimeter, and surface gravity data: GEM-T3, *J. Geophys. Res.*, **99**, 2815-2839, 1994.

McNutt, M. K., and K. M. Fischer, The South Pacific superswell, in *Seamounts, Islands, and Atolls*, edited by B. H. Keating, P. Fryer, R. Batiza, and G. W. Boehlert, *Geophysical Monograph Series*, *43*, pp. 25-34, AGU, Washington, D. C., 1987.

McNutt, M. K., and A. V. Judge, The superswell and mantle dynamics beneath the South Pacific, *Science*, **248**, 969-975, 1990.

McNutt, M. K., and L. Shure, Estimating the compensation depth of the Hawaiian swell with linear filters, *J. Geophys. Res.*, **91**, 13,915-13,923, 1986.

Minster, J. B., and T. H. Jordan, Present-day plate motions, *J. Geophys. Res.*, **83**, 5331-5354, 1978.

Müller, R. D., W. R. Roest, J.-Y. Royer, L. M. Gahagan, and J. G. Sclater, A digital map of the ocean floor, *Scripps Institution of Oceanography, SIO Reference Series, 93-30*, 1993.

National Geophysical Data Center, ETOPO-5 bathymetry/topography data, *National Oceanic and Atmospheric Administration, Boulder, CO, Data Announcement, 88-MGG-02*, 1988.

Parsons, B., and F. M. Richter, A relation between the driving force and geoid anomaly associated with mid-ocean ridges, *Earth Planet. Sci. Lett.*, **51**, 445-450, 1980.

Parsons, B., and J. G. Sclater, An analysis of the variation of ocean floor bathymetry and heat flow with age, *J. Geophys. Res.*, **82**, 803-827, 1977.

Richards, M. A., and B. H. Hager, Geoid anomalies in a dynamic earth, *J. Geophys. Res.*, **89**, 5987-6002, 1984.

Richards, M. A., and B. H. Hager, Effects of lateral viscosity variations on long-wavelength geoid anomalies and topography, *J. Geophys. Res.*, **94**, 10,299-10,313, 1989.

Sandwell, D. T., and W. H. F. Smith, Global marine gravity from ERS-1, Geosat and Seasat reveals new tectonic fabric, *Eos Trans. AGU*, **73**, 133, 1992.

Smith, W. H., On the accuracy of digital bathymetric data, *J. Geophys. Res.*, **98**, 9591-9603, 1993.

Stein, C. A., and S. Stein, A model for the global variation in oceanic depth and heat flow with lithospheric age, *Nature*, **359**, 123-129, 1992.

Su, W.-J., R. L. Woodward, and A. M. Dziewonski, Degree 12 model of shear velocity heterogeneity in the mantle, *J. Geophys. Res.*, **99**, 6945-6980, 1994.